Surrogate Models for Transonic Aerodynamics for Multidisciplinary Design Optimization

Molly Catherine Segee

Thesis submitted to the Faculty of the
Virginia Polytechnic Institute and State University
in partial fulfillment of the requirements for the degree of

Master of Science
in
Aerospace and Ocean Engineering

Joseph A. Schetz, Chair
Rakesh K. Kapania, Co-Chair
Pradeep Raj

April 14, 2016
Blacksburg, Virginia

Keywords: Transonic Aerodynamics, Multidisciplinary Design Optimization, Truss-braced Wings, Strut-braced Wings, Computational Fluid Dynamics, Response Surface, Surrogate Models, Artificial Neural Networks, Buffet Boundary

Surrogate Models for Transonic Aerodynamics for Multidisciplinary Design Optimization

Molly C. Segee

ABSTRACT

Multidisciplinary design optimization (MDO) requires many designs to be evaluated while searching for an optimum. As a result, the calculations done to evaluate the designs must be quick and simple to have a reasonable turn-around time. This makes aerodynamic calculations in the transonic regime difficult. Running computational fluid dynamics (CFD) calculations within the MDO code would be too computationally expensive. Instead, CFD is used outside the MDO to find two-dimensional aerodynamic properties of a chosen airfoil shape, BACJ, at a number of points over a range of thickness-to-chord ratios, free-stream Mach numbers, and lift coefficients. These points are used to generate surrogate models which can be used for the two-dimensional aerodynamic calculations required by the MDO computational design environment. Strip theory is used to relate these two-dimensional results to the three-dimensional wing. Models are developed for the center of pressure location, the lift curve slope, the wave drag, and the maximum allowable lift coefficient before buffet. These models have good agreement with the original CFD results for the airfoil. The models are integrated into the aerodynamic and aeroelastic sections of the MDO code.

Surrogate Models for Transonic Aerodynamics for Multidisciplinary Design Optimization

Molly C. Segee

GENERAL AUDIENCE ABSTRACT

Multidisciplinary design optimization (MDO), when applied to aircraft design, is a method of balancing the aerodynamic, structural, and control requirements of a design, which are often conflicting, to find an optimum design. This method has the potential to produce better, more efficient airplane designs as well as to save time and expense in the design process. Finding an optimum design with MDO requires the performance of many potential designs to be evaluated. The evaluation methods used must be quick and not require too many computational resources to keep the process from taking a long time. This greatly limits the aerodynamic calculations which can be done.

Most commercial airplanes have cruise Mach numbers in the transonic regime. This means that there are regions of both subsonic and supersonic flow around the airplane, as well as shocks. The differences in behavior of subsonic and supersonic flow as well as the sudden changes in the flow caused by shocks usually require the use of an evaluation method called computational fluid dynamics (CFD) to accurately evaluate the aerodynamic performance. However, CFD takes too long to be used for calculations in the MDO code.

Instead, CFD is used outside the MDO code to find the aerodynamic performance of an airfoil at several points over a range of thickness-to-chord ratios, free-stream Mach numbers, and lift coefficients. Next, functions are found which closely match the CFD results. These functions are then used by the MDO to calculate aerodynamic performance. This method allows aerodynamic calculations to be done in the MDO to better match real world physics without significantly changing the time required. This improves the accuracy and usefulness of designs found by the MDO.

Acknowledgments

I would like to thank to my advisors, Dr. Joseph A. Schetz and Dr. Rakesh K. Kapania, for all their support and guidance and for looking out for me during my time here. Thanks as well to Dr. Pradeep Raj, Dr. William Mason, Christopher Droney, and Chester Nelson for many helpful discussions and suggestions. This research was funded by NASA under a SMAART contract to the Boeing Company, so thanks to both NASA and Boeing for making this possible. I would also like to thank my fellow students, who showed me how things work at this school and who also made my time here more enjoyable. I would especially like to thank Wrik Mallik, who explained to me much of the research that this work is built off of. I also want to thank my boyfriend, Horatio Cowan IV, for believing in me when I felt overwhelmed and for moving all the way to Virginia. Lastly, I would like to thank my parents, Bruce and Cathy Segee, who taught me to value learning and who are the ones who got me interested in engineering in the first place.

Contents

List of Figures

List of Tables

Nomenclature

c	chord
C_l	two-dimensional lift coefficient
C_L	three-dimensional lift coefficient
$C_{l,max}$	maximum allowed sectional lift coefficient
C_m	two-dimensional quarter chord moment coefficient
C_d	two-dimensional drag coefficient
C_{dw}	two-dimensional wave drag coefficient
C_{DW}	three-dimensional wave drag coefficient
C_{DF}	three-dimensional skin friction drag coefficient
C_p	pressure coefficient
$\mathrm{Con}_{Cl_{max}}$	maximum sectional lift coefficient constraint
$f_{i,j}$	neural network activation function for layer i and node j
M	free-stream Mach number
M_{crit}	critical Mach number
M_L	local Mach number
M_{DD}	drag divergence Mach number
Re	Reynolds number
S	planform area
t/c	thickness-to-chord ratio
$w_{i,j,k}$	neural network weight for layer i, node j, and input k
x	distance from leading edge
$\bar{x}_{cp}$	chordwise center of pressure location
y	distance from fuselage
α	angle of attack
κ_a	Korn technology factor
Λ	sweep angle

Chapter 1

Introduction

1.1 Background

1.1.1 Truss-Braced and Strut-Braced Wings

Nearly all commercial transport aircraft since the 1950's have used a cantilever, low wing configuration. There have been considerable improvements in aircraft performance since then; however, with the exception of propulsion [6], there has been very little improvement in the aerodynamic performance of commercial transport aircraft since the 1960's [7] even as analysis and design tools have improved. It is likely that the aerodynamic performance of modern commercial transport aircraft is near the best possible for a cantilever, low wing configuration and that significant improvements will require alternative configurations.

One potential alternative configuration is the strut-braced wing (SBW) or truss-braced wing (TBW). A SBW has a strut which runs from the fuselage to the underside of the high wing and which helps to support the wing. A TBW is similar, but also has additional support members which connect the strut and the wing. This additional support for the wing allows a larger aspect ratio than a typical cantilever wing design, decreasing induced

drag, without a large increase in wing weight or thickness. The wave drag is also reduced when the wings are made thinner. This reduced wave drag also allows the wing sweep to be reduced. Reduced wing sweep on thin wings with reduced chords encourages laminar flow, which reduces parasitic drag [8].

A SBW configuration was first proposed by Pfenninger in the 1950's [9]. Pfenninger's proposed design had a lift to drag ratio greater than 40. However, its wingspan was larger than most airports can accommodate [1]. A picture of this design is shown in figure 1.1. In the 1970's, Boeing designed a military transport aircraft for a payload of 350,000 lb and a range of 10,000 nmi. It was found that a SBW design had potentially lower empty and gross weights, as well as reduced fuel consumption [10]. Two NASA studies of SBW aircraft showed reduced fuel weight [11] or increased range [12] compared to cantilever designs.

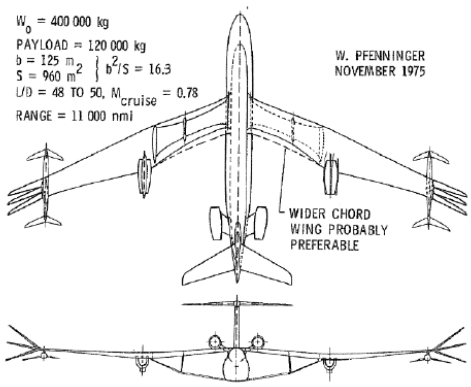

Figure 1.1: Pfenninger's proposed TBW airplane design [1]

More recent studies at Virginia Tech have shown the benefits of SBW and TBW configurations through multidisciplinary design optimization (MDO) analyses [13] [14] [15] [16] [17] [4] [2]. These studies were done for long-range and medium range transonic transports as part of NASA's Subsonic Ultra Green Aircraft Research (SUGAR) program, which focuses on reducing the environmental impact of future airplanes [18].

1.1.2 Transonic Aerodynamics

Transonic flow contains both regions of supersonic and regions of subsonic flow. This usually occurs at free-stream Mach numbers between 0.8 and 1.2 [19], and this mixture of subsonic and supersonic flow greatly complicates aerodynamic analyses. Despite these complications, most commercial airplanes have cruise Mach numbers in the transonic regime.

The free-stream Mach number at which supersonic flow first begins to appear on an airfoil is the critical Mach number. As the free-stream Mach number is increased past the critical Mach number, this region of supersonic flow grows. This region of supersonic flow changes the shape of the pressure distribution on the airfoil surface due to the differences in behavior of supersonic and subsonic flow as well as the presence of a shock terminating the region of supersonic flow. As a result, the Prandtl-Glauert compressibility corrections, which are given in equations 1.1 and 1.2, do not apply above the critical Mach number [19]. The lift and moment coefficients both change dramatically in the transonic regime, as do the center of pressure and the lift curve slope [20] [21].

$$C_l = \frac{C_{l,incompressible}}{\sqrt{1-M^2}} \tag{1.1}$$

$$C_m = \frac{C_{m,incompressible}}{\sqrt{1-M^2}} \tag{1.2}$$

The shocks in the flow also increase drag. Some of this increase is directly due to the shocks. However, the large pressure gradient caused by a shock also tends to cause boundary layer flow to separate, which also increases drag [19]. At some free-stream Mach number, there will be a large region of separated flow which causes a sharp increase in drag. This free-stream Mach number is the drag divergence Mach number. The following definition for the drag divergence Mach number is used here [22]:

$$\left.\frac{\partial C_{DW}}{\partial M}\right|_{M=M_{DD}} = 0.1 \tag{1.3}$$

1.1.3 Multi-Disciplinary Design Optimization

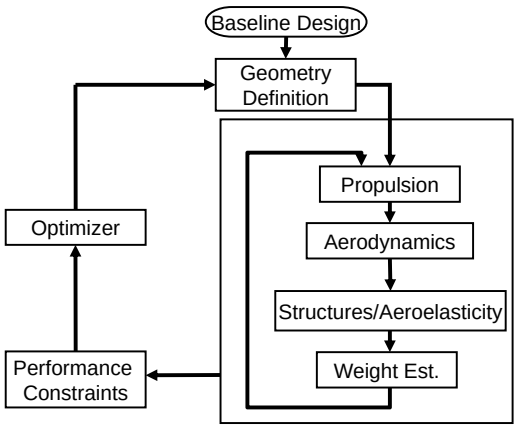

Figure 1.2: Virginia Tech MDO code outline [2] [3]

Virginia Tech has developed multi-disciplinary design optimization (MDO) code focused on the design of SBWs and TBWs [13] [14] [15] [16] [17] [4] [2]. MDO allows variables to be manipulated and designs to be evaluated in multiple disciplines simultaneously [23]. This allows the design to be optimized based on some objective function, typically take-off gross weight (TOGW) or fuel consumption. MDO is useful in the design of TBWs and SBWs due to the high degree of coupling between the aerodynamics and the structures [13]. The Virginia Tech MDO code is made up of several analysis and optimization nodes, called wrappers. Each of these wrappers consists of C++ and FORTRAN scripts [2]. These scripts are connected together through Phoenix Integration's ModelCenter [24]. Figure 1.2 shows how the different wrappers are connected. This work will focus on the aerodynamic wrapper and the aeroelastic section of the structures/aeroelasticity wrapper.

Aerodynamic Wrapper

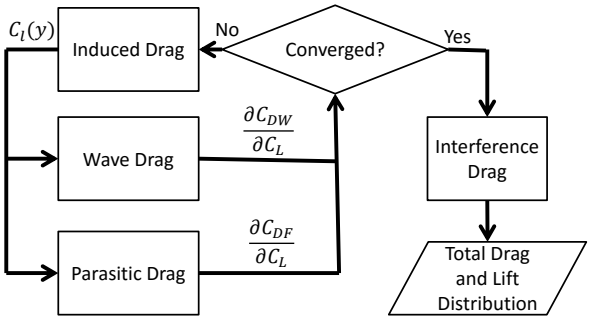

Figure 1.3: Virginia Tech MDO aerodynamic wrapper outline [4]

Strip theory is used in the aerodynamic wrapper to relate the three-dimensional lift distribution on the wing to two-dimensional aerodynamic coefficients. The wing is divided into strips which are assumed to have a constant lift coefficient. The two-dimensional lift and drag coefficient for each wing strip can be found by making the following corrections for wing sweep.

$$C_l = \frac{C_L}{\cos^2 \Lambda} \tag{1.4}$$

$$C_d = \frac{C_D}{\cos^3(\Lambda)} \tag{1.5}$$

Similar corrections can be made for the thickness-to-chord ratio and the free-stream Mach number.

$$(t/c)_{2D} = \frac{(t/c)_{3D}}{\cos \Lambda} \tag{1.6}$$

$$M_{2D} = M_{3D} \cos \Lambda \tag{1.7}$$

The aerodynamic wrapper can be divided into four sections: induced drag calculation, parasitic drag calculation, wave drag calculation, and interference drag calculation. The structure of the aerodynamic wrapper and the way that information is shared between sections is shown in figure 1.3. The induced drag module uses a discrete vortex method to calculate the induced drag in the Trefftz plane. It provides the load distribution corresponding to the minimum drag. This requires the sensitivities of the wave drag and the parasitic drag to changes in lift to be known. An iterative approach is used in which a lift distribution is found, then the sensitivities of the wave drag and parasitic drag coefficients to changes in the lift coefficient are updated. This process is repeated until the lift distribution converges. The interference drag calculation is not included in these iterations, as it typically contributes to less than 2% of the total drag. Additional constraints are also placed on the lift distribution which limit the maximum sectional lift coefficient to $C_{l,max}$. Further details about the induced drag calculation can be found in [4]. The pitching moment about the center of gravity of the entire configuration can be specified in the induced drag calculations, although this is not required.

The parasitic drag is dependent on the amount of laminar flow. To estimate the transition Reynolds number, data from Braslow and Collier relating transition Reynolds number to sweep is used [25]. A laminar flow technology factor is included which allows this to be modified. The Eckert Reference Temperature Method is used to find the skin friction for the regions with laminar flow, and the Van Driest II formula is used to find the skin friction for the regions with turbulent flow. Form factors for wings and bodies are used to include the effects of friction [13].

The lift distribution found from the induced drag calculation is used to determine the wave drag. First, the wing is divided into strips which are assumed to have a constant lift and chord. The wave drag for each strip is calculated, then summed to find the total wave drag for the wing. In previous studies, the Virginia Tech MDO code has found the wave drag for each strip using empirical relations [26]. First, the drag divergence number for each airfoil section is found using the Korn equation extended to include wing sweep [27].

$$M_{DD} = \frac{\kappa_a}{\cos\Lambda} - \frac{t/c}{\cos^2\Lambda} - \frac{C_L}{10\cos^3\Lambda} \tag{1.8}$$

The wave drag is found from the drag divergence Mach number using an empirical approximation from Lock which relates the wave drag to the free-stream Mach number and the critical Mach number [28].

$$C_{DW} = 20(M - M_{crit})^4 \tag{1.9}$$

By relating (1.9) to the definition of the drag divergence Mach number:

$$\left.\frac{\delta C_{DW}}{\delta M}\right|_{M=M_{DD}} = 0.1 \tag{1.10}$$

the critical Mach number can be found.

$$M_{crit} = M_{DD} - \left(\frac{0.1}{80}\right)^{1/3} \tag{1.11}$$

This critical Mach number can then be used with equation 1.9 to find the wave drag. The wave drag for the total wing is [13]:

$$C_{DW} = 20(M - M_{crit})^4 \frac{S_{strip}}{S_{ref}} \text{ for } M > M_{crit} \tag{1.12}$$

The interference drag is calculated based on models fit to results from computational fluid dynamics (CFD) simulations. The interference drag caused by the strut-wing intersection is estimated as a function of thickness-to-chord ratio, Reynolds number, and the dihedral angle between the strut and the wing. This is done with a third-order polynomial fit to CFD data. [29]. The interference drag caused by the intersection of the struts is estimated with second-order polynomial which is a function of thickness-to-chord ratio and the intersection

angle. Two separate models were made, the first for a free-stream Mach number of 0.8 and the second for a free-stream Mach number of 0.85 [30].

Aeroelastic Wrapper

The flutter analysis method used by the Virginia Tech MDO code is outlined in [3]. The k or $V-g$ method is used, with Theodorson's method used for the unsteady aerodynamic analysis, including the lift curve slope. The Prandtl-Glauert correction factor for swept wings is used for the compressibility effects. The flutter analysis calculations use the center of pressure location, which has been shown to move aft as the free-stream Mach number is increased [20]. To include this effect, the center of pressure is crudely assumed to vary linearly from 25% of the chord at a free-stream Mach number of 0.4 to 40% of the chord at a free-stream Mach number of 0.9.

1.1.4 Artificial Neural Networks

Artificial neural networks are a method of modeling unknown functions. This type of model was originally inspired by the structure of the brain [31]. Neural networks do not require assumptions to be made about the relationship between the input and the output [31]. They are also capable of approximating any continuous function [32]. Neural networks consist of a system of interconnected nodes. An example diagram of a neural network is shown in figure 1.4. The input to each node is multiplied by weights, shown with arrows, then goes through an activation function, f. The models presented here use hyperbolic tangent functions for the activation functions because that is what is used by the statistical software

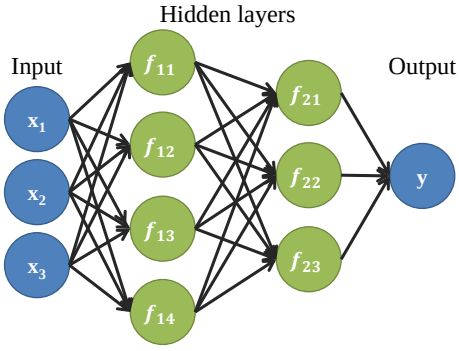

Figure 1.4: Example diagram of a neural network

JMP, which was used to train these neural networks. Other types of activation functions are possible. The activation function output becomes the input for the next layer of nodes. The weights between the nodes are found by training the neural network with known inputs and associated outputs for the function which is being approximated. The weights are adjusted to minimize the error between the neural network output and the output for the training samples [33]. The number of input nodes is the same as the number of input variables for the neural network. The number of nodes in the hidden layers must be chosen, as well as the number of hidden layers. There is not currently a method for determining the optimum number of hidden nodes and layers [31]. Generally, networks with more nodes can approximate functions more closely, but they also require more computations to find an output. There is also a risk of over-fitting if there is noise in the data. Using more than one layer of hidden nodes can sometimes reduce the overall number of nodes required [34].

1.2 Problem Definition

Multidisciplinary design optimization requires a large number of designs to be evaluated while searching for an optimum solution. This typically limits the aerodynamic evaluation to simplified methods and empirical relations, which do not always reflect real world physics, particularly in the transonic regime. It is desired to improve on these methods without significantly increasing the computational expense of the aerodynamic evaluations in the Virginia Tech MDO code. Running CFD calculations within the MDO code would require too many computational resources to be useful in most design applications [35].

1.3 Proposed Solution

CFD is used to create a database of two-dimensional aerodynamic coefficients and related values to be used in the strip theory formulation in the VT MDO code. This is done for

a BACJ airfoil shape, which is representative of a typical modern supercritical airfoil. The database is created for the range of free-stream Mach numbers, thickness-to-chord ratios, and lift coefficients likely to be used by the Virginia Tech MDO code. Surrogate models are fit to the database results which can be directly used by the MDO to predict values at any point within the range of database values. Artificial neural networks are used as surrogate models due to their ability to approximate any continuous function [32] and the fact that they do not require any initial assumptions to be made about the data [31]. Models are created for the lift curve slope, the center of pressure location, the wave drag, and the maximum allowable lift coefficient before buffet. An empirical relationship from [5] which relates the local Mach number before the shock and the shock location to buffet onset is used to determine which cases will experience buffet.

Chapter 2

Database Generation

2.1 Database Ranges

The ranges of the quantities covered in the current database were selected as appropriate for use for transonic cantilever, SBW and TBW aircraft in the Virginia Tech MDO code or in similar codes.

The BACJ airfoil has a thickness-to-chord ratio of 10%. Two other similar airfoils with thickness-to-chord ratios of 8% and 6% were created. Previous studies done with the Virginia Tech MDO code have had thickness-to-chord ratios close to this range when adjusted for wing sweep [13] [16] [14] [15] [17] [22]. To create the thinner airfoils, the thickness perpendicular to the chord was scaled by moving the upper and lower surface points toward the midpoint between the two surfaces.

The database covers free-stream Mach numbers from 0.7 to 0.95. The higher Mach numbers are needed for flutter calculations.

The database results cover a range of lift coefficients from 0 to 0.8. The Virginia Tech MDO code limits the two-dimensional lift coefficient to some maximum, usually 0.7 or 0.8. The flow solver used, SU2, takes angle of attack as an input. Results are obtained for angles of

attack in steps of 1.5° until the entire range of lift coefficients has been covered.

2.2 Methodology

Steady, two-dimensional RANS equations were used to find the lift, drag, and moment coefficients of the airfoil. A Spalart-Allmaras turbulence model was used, and all cases were run at a Reynolds number of 6×10^6. The flow solver used was SU2. More information about this solver can be found in [36] and [37]. The pressure distribution on the airfoil surface is also obtained, which can be integrated to find the wave drag.

Inviscid, Euler equations were initially used to generate this database. However, it was found that there was a large difference between the viscous and the inviscid behavior of this airfoil. Plots of the pressure coefficient around the airfoil for a lift coefficient of 0.335, a free-stream Mach number of 0.8, and a thickness-to-chord ratio of 10% is shown in figure 2.1. Figure 2.1 (a) shows the flowfield found using Euler equations, and figure 2.1 (b) shows the flowfield found using RANS equations. It can be seen that the Euler equations predict a stronger shock which is further aft than is predicted by the RANS equations. The Euler results also have a shock on the lower surface which does not appear in the RANS results. As a result, the inviscid results predict a quarter-chord moment coefficient which is much higher than the moment coefficient predicted by the viscous results. This causes the center of pressure to move from 86% of the chord for the inviscid results to 70% of the chord for the viscous results. Because of the large difference in results, viscous RANS equations were used to generate the database for the MDO.

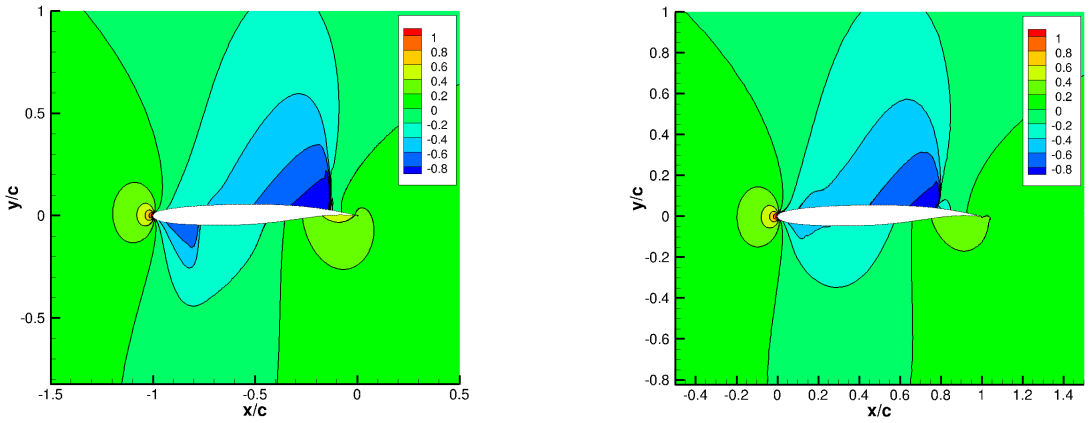

(a) Euler (b) RANS

Figure 2.1: Pressure coefficient results for 10% thickness-to-chord ratio BACJ airfoil at a lift coefficient of 0.335 and a free-stream Mach number of 0.8

2.3 Meshes

A separate mesh was made for each of the three thickness-to-chord ratios used. The meshes were made in Pointwise. The 10% thickness-to-chord ratio mesh is shown in figure 2.2; the other meshes used look similar. Each mesh consists of three regions. The first is a structured 1600×35 region at the airfoil surface to resolve the boundary layer. The insert in figure 2.2 shows this region in greater detail. The cell spacing at the airfoil surface is 2.9×10^{-6} which results in y+ values near 1. The second region is a finer unstructured region to resolve the shocks. This region is circular with a radius of 1.5 chord lengths centered on the trailing edge and contains 6×10^4 cells. The rest of the mesh consists of a coarser, unstructured region containing 9×10^3 cells. The cell counts given here are approximate, since the exact number of cells varies between the three meshes used. The front of these meshes has a radius of 20 chord lengths, and the meshes extended 20 chord lengths behind the airfoil.

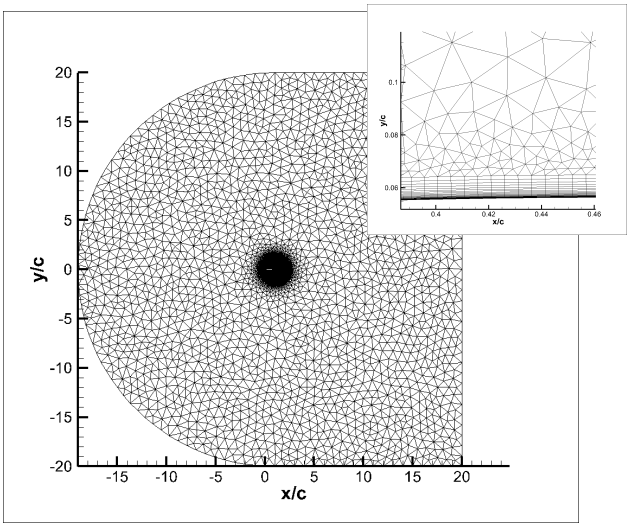

Figure 2.2: Mesh for 10% thickness-to-chord ratio BACJ airfoil

All three meshes used were found to be fine enough for mesh independent results. This was checked by comparing the results to results obtained from a mesh with approximately 4 times as many cells. This was done at the highest lift coefficient for both the highest and lowest Mach number for each thickness-to-chord ratio, for a total of six cases. The difference between the results for the two meshes is shown in Figure 2.3 (a), and the percent difference in the results is shown in Figure 2.3 (b).

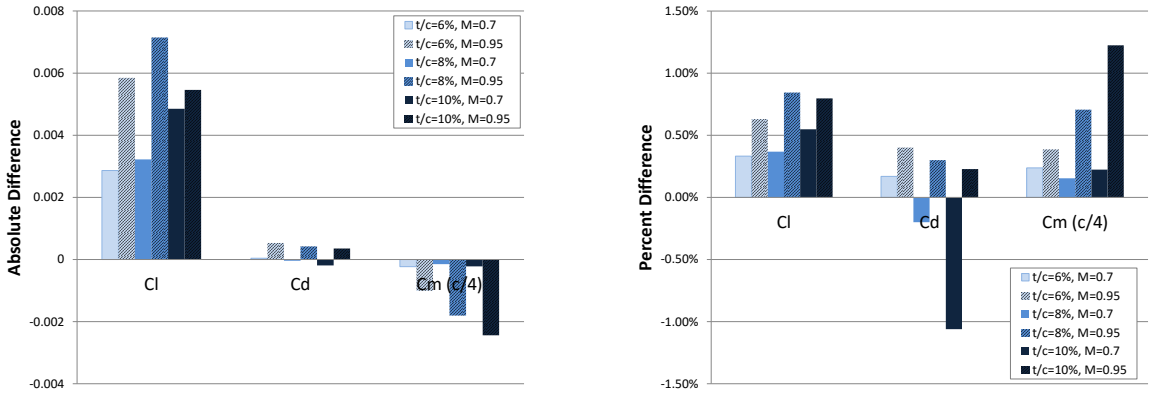

(a) Absolute difference in results

(b) Percent difference in results

Figure 2.3: Comparison of coarser and finer mesh CFD results for a BACJ airfoil

The CFD runs were done in parallel on six cores. The time required by each run ranged from 3.5 to 8.5 hours, though most cases took around 5 hours.

2.4 CFD Database Results

The pressure coefficient around a 10% thickness to chord ratio BACJ airfoil at an angle of attack of 1.5° is shown in figure 2.4 for free-stream Mach numbers of 0.7, 0.8, and 0.9. At a free-stream Mach number of 0.7, there is only a small region of supersonic flow near the leading edge of the airfoil. As the free-stream Mach number is increased to 0.8, this region grows. The sudden increase in pressure caused by the shock at the end of this region is clearly visible in figure 2.4 (b) at 75% of the chord. For a free-stream Mach number of 0.9, there is a shock on both the upper and lower surface of the airfoil. There is also a drop in the lift coefficient from 0.66 to 0.09 due to the low pressure flow around the lower surface of the airfoil.

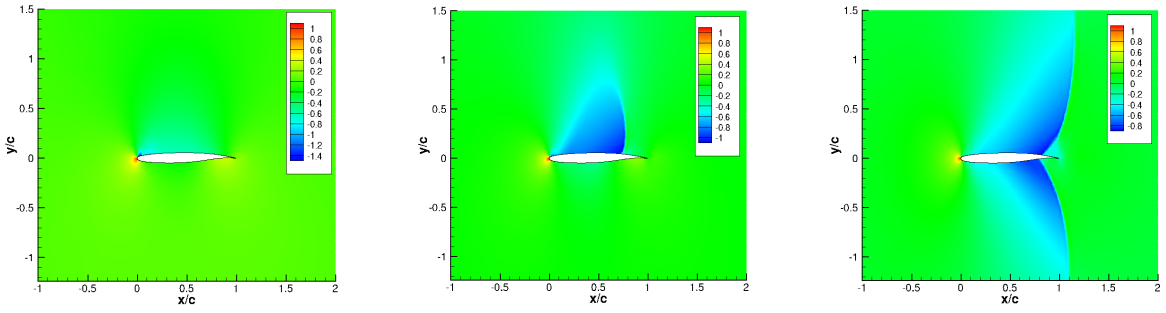

(a) Free-stream Mach number of 0.7, lift coefficient 0f 0.6193

(b) Free-stream Mach number of 0.8, lift coefficient 0f 0.6591

(c) Free-stream Mach number of 0.9, lift coefficient 0f 0.0928

Figure 2.4: Pressure coefficient results for BACJ airfoil with a thickness-to-chord ratio of 10% and an angle of attack of 1.5°

2.4.1 Lift Coefficient Results

The lift coefficient for the BACJ airfoil vs angle of attack is shown in figure 2.5. The lift coefficient is almost constant with thickness-to-chord ratio for the 0.7 free-stream Mach number cases. This is likely due to the fact that these cases have either small or no regions of locally supersonic flow. The lift coefficient increases as the free-stream Mach number is increased from 0.7 to 0.8, then decreases as the free-stream Mach number is increased further until a Mach number of 0.9. At some point, as the free-stream Mach number is increased, the lift coefficient stops decreasing. This happens sooner for the airfoils with a higher thickness-to-chord ratio and for lower angles of attack.

The lift curve slope is almost constant at a free-stream Mach number of 0.7 for all the cases. As the free-stream Mach number is increased, the presence of shocks and flow separation cause the slope to vary with lift. When the free-stream Mach number is increased to 0.95, the upper surface shock is near the trailing edge. The shock does not move as the lift is varied, and the region of separated flow after the shock is small. As a result, the lift curve slope is essentially constant with angle of attack for cases where the free-stream Mach number is 0.95.

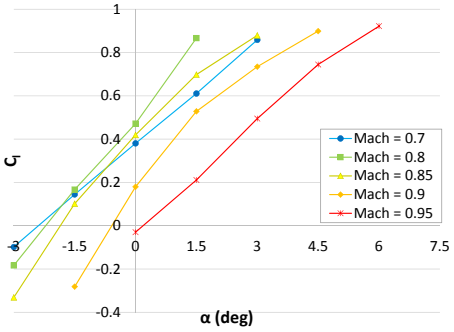

(a) Thickness to chord ratio of 6%

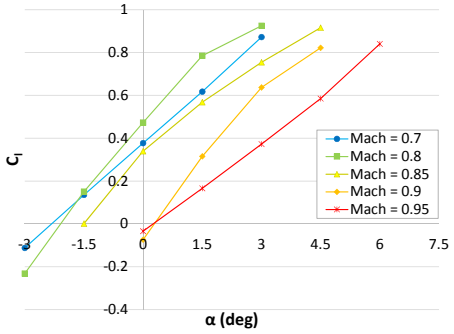

(b) Thickness to chord ratio of 8%

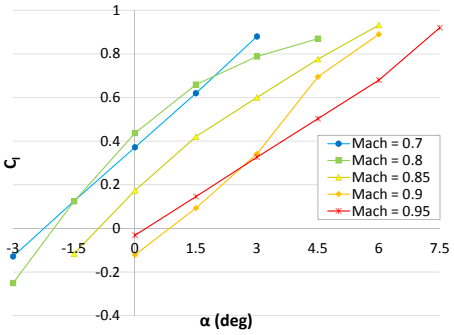

(c) Thickness to chord ratio of 10%

Figure 2.5: BACJ airfoil lift coefficient vs. angle of attack for free-stream Mach numbers from 0.7 to 0.95

2.4.2 Drag Coefficient Results

The drag coefficient as a function of the lift coefficient for the airfoil is shown in figure 2.6. It can be seen that the drag increases with lift, free-stream Mach number, and thickness-to-chord ratio, as would be expected.

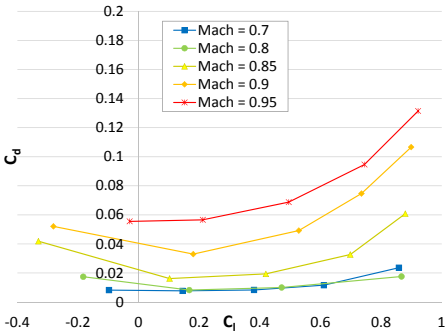

(a) Thickness to chord ratio of 6%

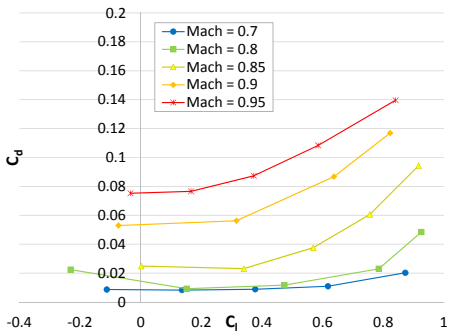

(b) Thickness to chord ratio of 8%

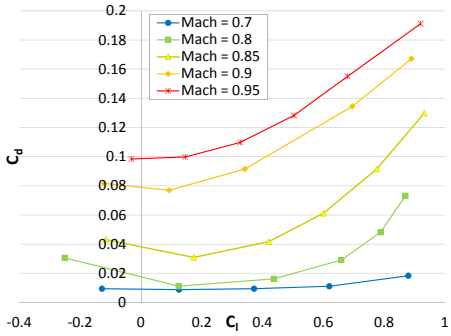

(c) Thickness to chord ratio of 10%

Figure 2.6: BACJ airfoil drag coefficient vs. lift coefficient for free-stream Mach numbers from 0.7 to 0.95

The drag polars are shown in figure 2.7. The results are grouped by free-stream Mach number, and a separate line is shown for each thickness-to-chord ratio. Note that the axes in the sub-figures are not all the same length. At lower free-stream Mach numbers, the drag coefficient is lower and less dependent on thickness-to-chord ratio than it is at higher free-stream Mach numbers. For most cases, the drag increases with thickness-to-chord ratio. This is because the thicker airfoils disturb the flow more and cause stronger shocks. It is interesting to note, however, that at high lift coefficients and a free-stream Mach number of 0.7, the drag decreases with thickness-to-chord ratio. This is because the thinner airfoils have a smaller leading edge radius. This causes the flow to accelerate more at the leading edge, which causes stronger shocks in this region.

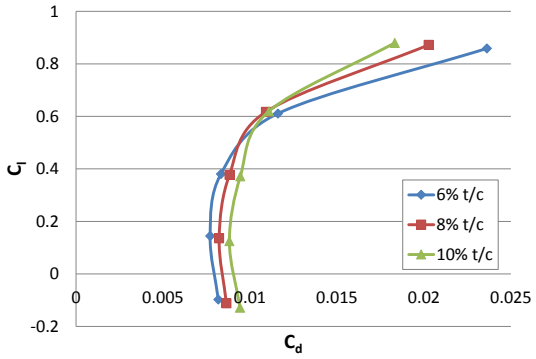

(a) Free-stream Mach number of 0.7

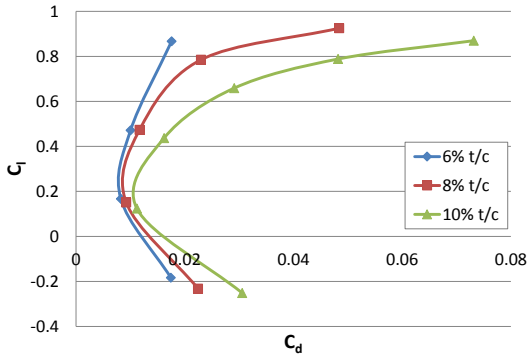

(b) Free-stream Mach number of 0.8

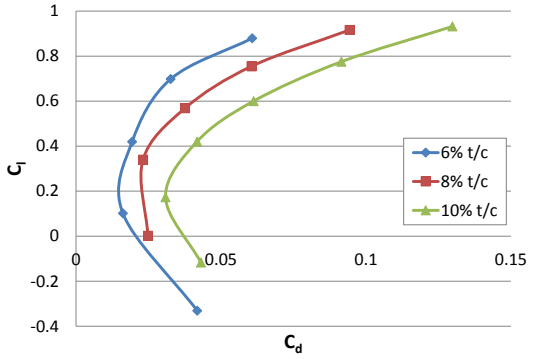

(c) Free-stream Mach number of 0.85

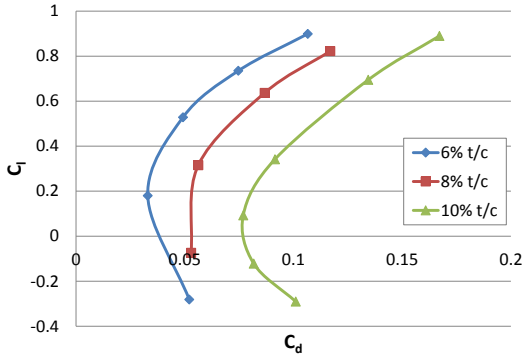

(d) Free-stream Mach number of 0.9

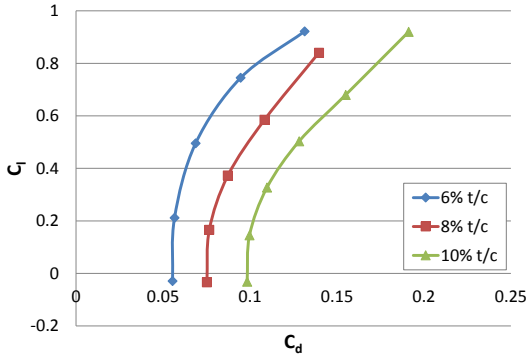

(e) Free-stream Mach number of 0.95

Figure 2.7: BACJ airfoil drag polar for thickness-to-chord ratios of 6%, 8%, and 10%

2.4.3 Wave Drag Coefficient Results

The wave drag is found from the CFD results by integrating the pressure coefficients on the surface of the airfoil. The trapezoidal rule for numerical integration was used. This is shown in equation 2.1.

$$C_{dw} = \cos\alpha \sum \Delta y_i \frac{C_{p,i} + C_{p,i-1}}{2} - \sin\alpha \sum \Delta x_i \frac{C_{p,i} + C_{p,i-1}}{2} \tag{2.1}$$

Where i increases clockwise around the airfoil. The CFD results for wave drag are shown in figure 2.8 as a function of lift coefficient. These results are similar to the total drag results, but are shifted down by 50 to 75 counts.

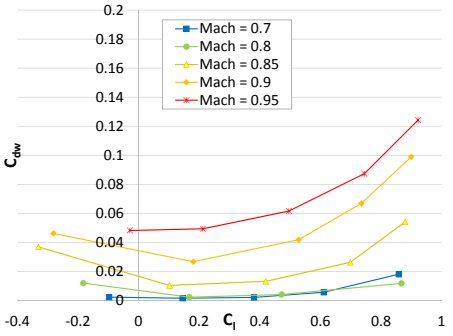

(a) Thickness to chord ratio of 6%

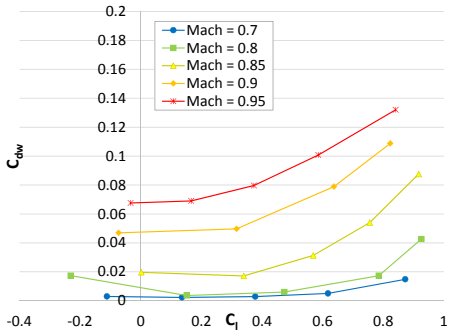

(b) Thickness to chord ratio of 8%

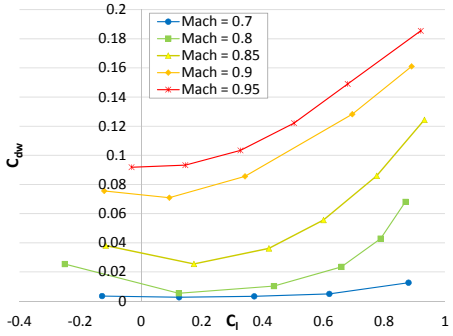

(c) Thickness to chord ratio of 10%

Figure 2.8: BACJ airfoil wave drag coefficient vs. lift coefficient for free-stream Mach numbers from 0.7 to 0.95

Figure 2.9 compares the CFD results to the Korn equation and Lock's fourth power law method used previously by the MDO. A Korn technology factor of 0.8756 was used. At free-stream Mach numbers of 0.85 or less, the two methods have similar results, but at higher free-stream Mach numbers the Korn/Lock method is overly pessimistic.

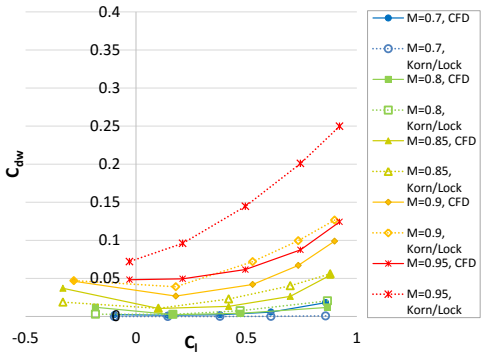

(a) Thickness to chord ratio of 6%

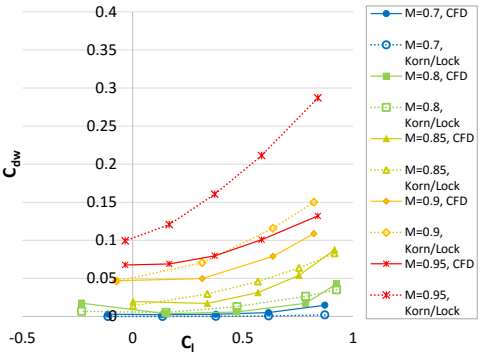

(b) Thickness to chord ratio of 8%

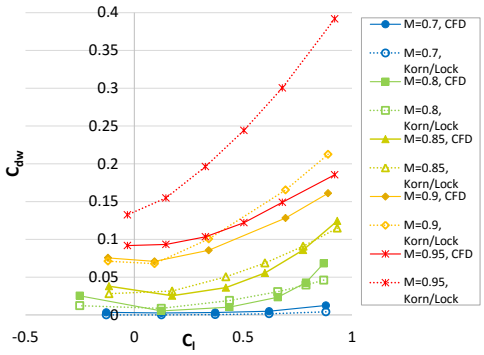

(c) Thickness to chord ratio of 10%

Figure 2.9: BACJ airfoil CFD wave drag results compared to Korn equation and Lock's fourth power law results with a technology factor of 0.8756

2.4.4 Moment Coefficient Results

The quarter-chord moment coefficient as a function of the lift coefficient is shown in figure 2.10. The moment is almost constant for a free-stream Mach number of 0.7, and changes very

little with thickness-to-chord ratio. The moment changes as the Mach number is increased, and the slope of the moment coefficient also tends to change with lift. This might be caused by the appearance and movement of shocks in the flow. At a free-stream Mach number of 0.95, the slope of the moment coefficient is almost constant. At this Mach number, the shocks are near the trailing edge of the airfoil, and they do not move much as the lift coefficient is changed.

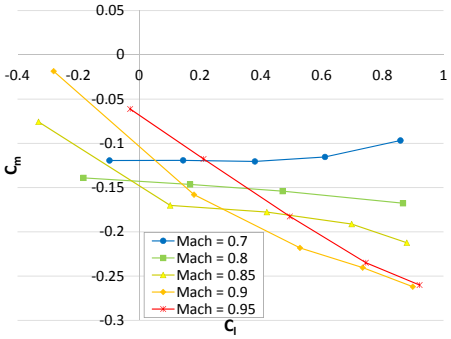

(a) Thickness to chord ratio of 6%

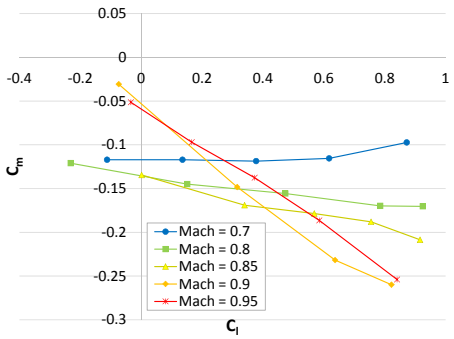

(b) Thickness to chord ratio of 8%

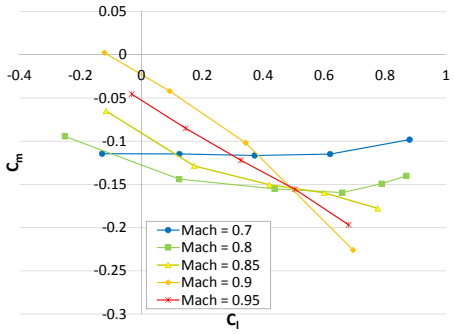

(c) Thickness to chord ratio of 10%

Figure 2.10: BACJ airfoil moment coefficient vs. lift coefficient for free-stream Mach numbers from 0.7 to 0.95

2.5 Validation Dataset

Surrogate models are fit to the CFD results to be used by the MDO for interpolation. To ensure that these models give accurate results, a series of CFD runs were done to create a validation dataset. This validation dataset is used to check the accuracy of the models used by the MDO, but is not used to generate these models. The results at each point in this validation dataset are compared to the results predicted by the models used by the MDO to ensure that they are similar.

Points in the validation dataset are chosen to be between points used to generate the surrogate models used by the MDO. Thickness-to-chord ratios of 7% and 9%, free-stream Mach numbers of 0.75, 0.825, and 0.875, and angles of attack of 1° and 2° are used for a total of 12 cases. The lift coefficient results for these points are shown in figure 2.11. The lift coefficient increases with angle of attack, as would be expected; however, the sensitivity of the lift coefficient to changes in angle of attack varies from case to case. This is similar to the behavior of the lift coefficient in the database results shown in figure 2.5.

The 7% thickness-to-chord ratio airfoil has an increase in lift coefficient when the free-stream Mach number is increased from 0.75 to 0.825, while the 9% thickness-to-chord ratio airfoil has a drop in lift coefficient. The lift coefficient drops when the free-stream Mach number is increased to 0.875 for both cases, although the drop is more dramatic for the 9% thickness-to-chord ratio airfoil. These variations of lift coefficient with free-stream Mach number agree with the results in figure 2.5.

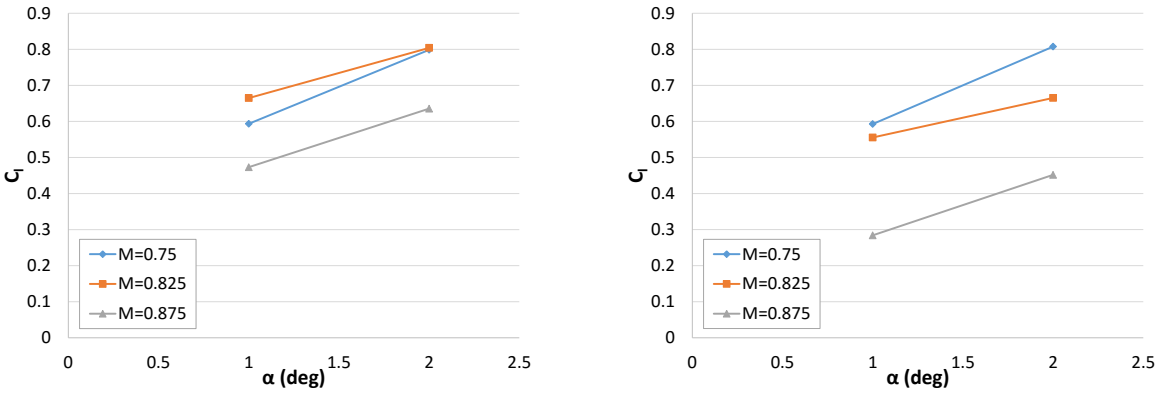

(a) Thickness to chord ratio of 7% (b) Thickness to chord ratio of 9%

Figure 2.11: BACJ airfoil lift coefficient vs. angle of attack for free-stream Mach numbers from 0.75 to 0.875

The drag coefficient results for the validation dataset are shown in 2.12. As was shown in the results in figure 2.6, the drag tends to increase with free-stream Mach number, lift coefficient, and thickness-to-chord ratio.

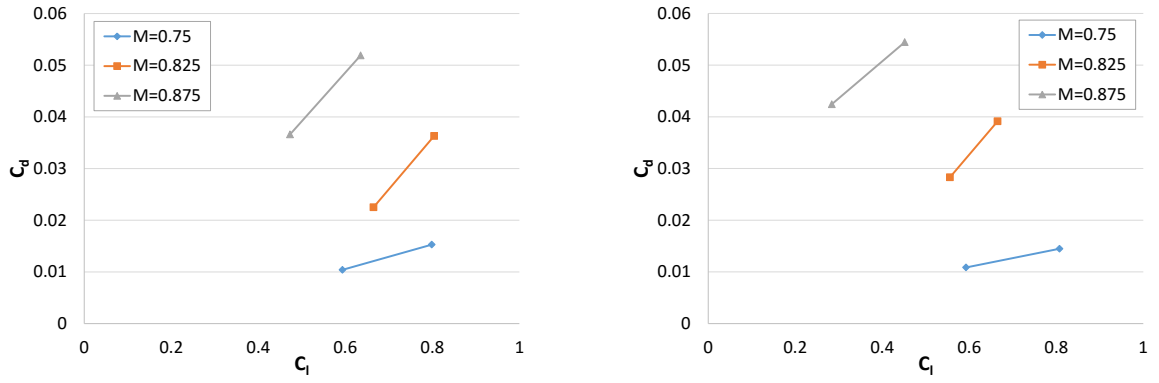

(a) Thickness to chord ratio of 7% (b) Thickness to chord ratio of 9%

Figure 2.12: BACJ airfoil drag coefficient vs. lift coefficient for free-stream Mach numbers from 0.75 to 0.875

The moment coefficient results for the validation dataset are shown in 2.13. For a free-stream

Mach number of 0.75, the moment coefficient does not change much with thickness-to-chord ratio. As the free-stream Mach number is increased further, the moment coefficient changes more with thickness-to-chord ratio. These results seem to show similar behavior to those shown in figure 2.10, although it is difficult to draw conclusions from so few points.

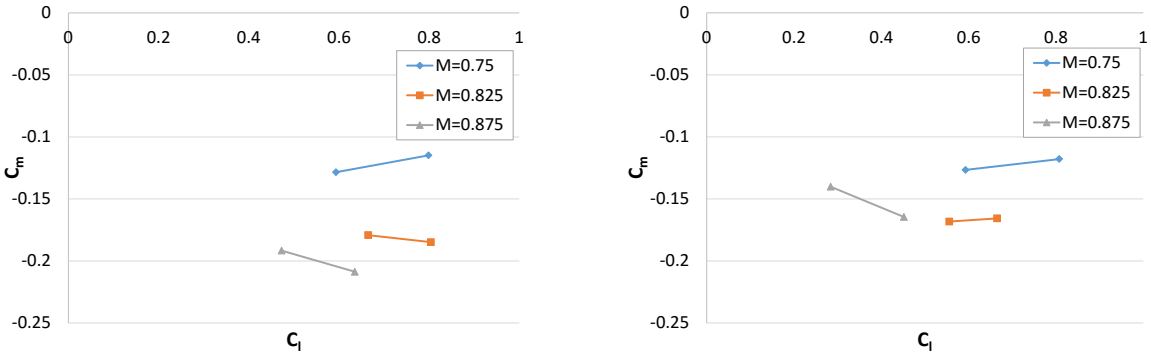

(a) Thickness to chord ratio of 7%

(b) Thickness to chord ratio of 9%

Figure 2.13: BACJ airfoil moment coefficient vs. lift coefficient for free-stream Mach numbers from 0.75 to 0.875

Chapter 3

Buffet Boundary Model

3.1 Background

Buffet is wing vibration caused by unsteadiness in the flow caused by a region of separated flow behind a shock [38]. Buffet is one of the major constraints when designing an aircraft [5], and designs should not buffet when the lift is increased to 1.3 times the cruise lift coefficient. Oscillations in the separated flow behind a shock are not considered buffet unless there is sufficient interaction with the structure to allow the oscillations to be felt by the pilot [5]. As a result, buffet boundary predictions are often highly empirical [38].

Figure 3.1 shows an empirical correlation for buffet onset. This correlation predicts buffet onset as a function of shock position and the local Mach number ahead of the shock. There are two lines, corresponding to Reynolds numbers of 10×10^6 and 30×10^6. If the shock position and local Mach number ahead of the shock are on or over this line, it is likely that there will be buffet. Points below these lines are not likely to buffet. These correlations only extend to a shock position of 70% of the chord. When shocks occur beyond this point, it is not likely that there will be enough interaction with the structure to cause buffet.

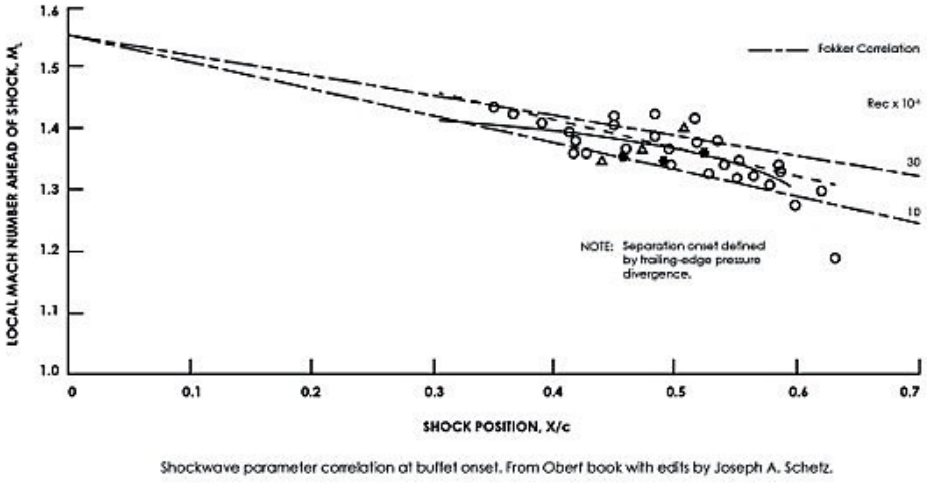

Figure 3.1: Empirical correlation for buffet onset, from reference [5]

3.2 Model Description

Several CFD cases were run for free-stream Mach numbers between 0.7 and 0.8 to determine how the maximum lift before buffet varies with free-stream Mach number. At a free-stream Mach number of 0.8, all the cases had a shock location greater than 70% of the chord. The shock location and local Mach number before the shock for the airfoil for each case were compared to the empirical buffet boundary in figure 3.1. The correlation for a Reynolds number of 10×10^6 was used. When a case was found which was on or just below the buffet boundary, the lift coefficient was taken as the maximum lift coefficient before buffet for that free-stream Mach number and thickness-to-chord ratio. These points are shown in figure 3.2. Points which have a shock at a location 70% of the chord or greater are marked with black circles. There is not likely to be enough interaction with the structure to cause buffet when the shock location is greater than 70% of the chord. The MDO imposes a limit on the two-dimensional lift coefficient for each wing strip. This limit can be varied, but it has always been kept below 0.8. Designs from the MDO should not experience buffet when the lift coefficient is increased to 1.3 times the cruise lift coefficient. This means that if the buffet

limit for the lift coefficient is greater than $1.3 \times 0.8 = 1.04$ it will have no effect on the design.

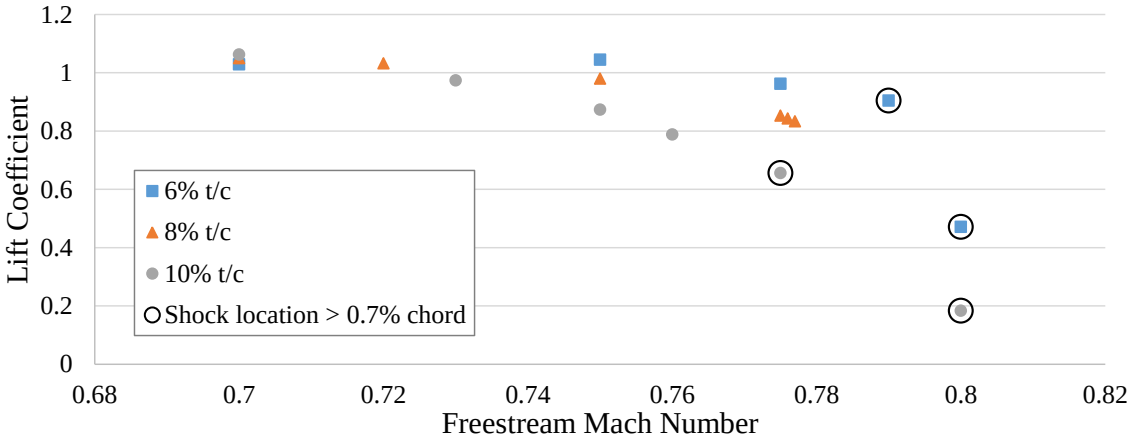

Figure 3.2: Maximum lift coefficient before buffet for a BACJ airfoil

Two models were made from the data shown in figure 3.2. The first models the maximum lift coefficient before buffet as a function of free-stream Mach number and thickness-to-chord ratio. To create this model, a neural network with one layer of three nodes is used. This number of nodes was found to fit the data well without being too large or requiring too many computations. Over-fitting was also a concern, as the points shown in figure 3.2 were not all directly on the buffet boundary. A diagram of this neural network is shown in figure 3.3.

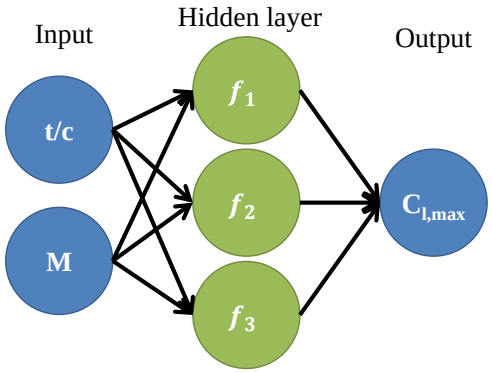

Figure 3.3: Diagram of neural network for maximum lift coefficient before buffet onset for a BACJ airfoil

Hyperbolic tangent functions are used as the activation functions in the hidden layer. This is shown in equation 3.1.

$$f_i = \tanh\left(\frac{1}{2}\left(w_{1,i,0} + w_{1,i,1}\frac{t}{c} + w_{1,i,2}M\right)\right) \tag{3.1}$$

The output is given by equation 3.2.

$$C_{l,max} = w_{2,0} + \sum_{i=1}^{4} w_{2,i} f_i \tag{3.2}$$

The weights from equations 3.1 and 3.2 are given in table 3.1.

Table 3.1: Maximum lift coefficient before buffet neural network weights

(a) Input layer

$w_{1,1,0}$	-85.77025738
$w_{1,1,1}$	80.8123999
$w_{1,1,2}$	102.637824
$w_{1,2,0}$	-70.94695257
$w_{1,2,1}$	72.94859294
$w_{1,2,2}$	83.89124589
$w_{1,3,0}$	-249.7347216
$w_{1,3,1}$	-1.354900618
$w_{1,3,2}$	309.6353676

(b) Output

$w_{2,0}$	-0.820250956
$w_{2,1}$	0.490373788
$w_{2,2}$	-0.780310264
$w_{2,3}$	-1.578030728

The maximum lift coefficient before buffet onset predicted with this neural network is plotted against free-stream Mach number in figure 3.4. This is done for thickness-to-chord ratios between 6% and 10%. This model has a root-mean-squared error of 0.0099 when compared to the original points shown in figure 3.2. At a free-stream Mach number of 0.7, the maximum lift coefficient before buffet is almost constant with thickness-to-chord ratio between 1.03 and

1.06. As the free-stream Mach number is increased, the maximum lift coefficient decreases. The maximum lift coefficient decreases faster for airfoils with higher thickness-to-chord ratios than it does for airfoils with lower thickness-to-chord ratios. This is expected because thicker airfoils disturb the flow more and cause stronger shocks.

The 10% thickness-to-chord ratio airfoil has some strange behavior at free-stream Mach numbers between 0.77 and 0.8. The slope in this region does not decrease as smoothly as it does for other thickness-to-chord ratios. By comparing figure 3.4 to figure 3.2, it can be seen that there are not many data points in this region. This likely causes the model to be less accurate at this location. However, it can be seen in figure 3.2 and it will be shown more clearly later, that in this region the shock location is beyond 70% of the chord. As a result, it is unlikely that there will be enough interaction with the structure to cause buffet.

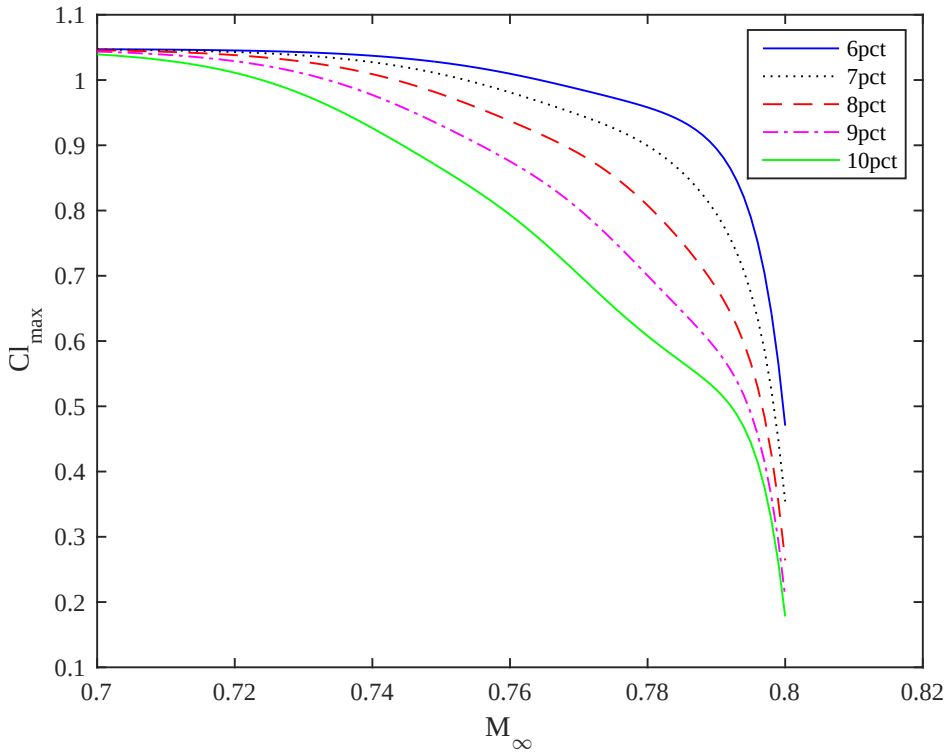

Figure 3.4: Maximum lift coefficient before buffet onset vs free-stream Mach number for a BACJ airfoil

The second model developed from the data shown in figure 3.2 predicts the free-stream Mach number at which the shock location will be 70% of the chord. The first step in creating this model is to determine at what free-stream Mach number the shock will be at 70% of the chord for each thickness-to-chord ratio. While the shock location is less than or close to 70% of the chord, the shock location is found to vary almost linearly with free-stream Mach number. This can be seen in figure 3.5.

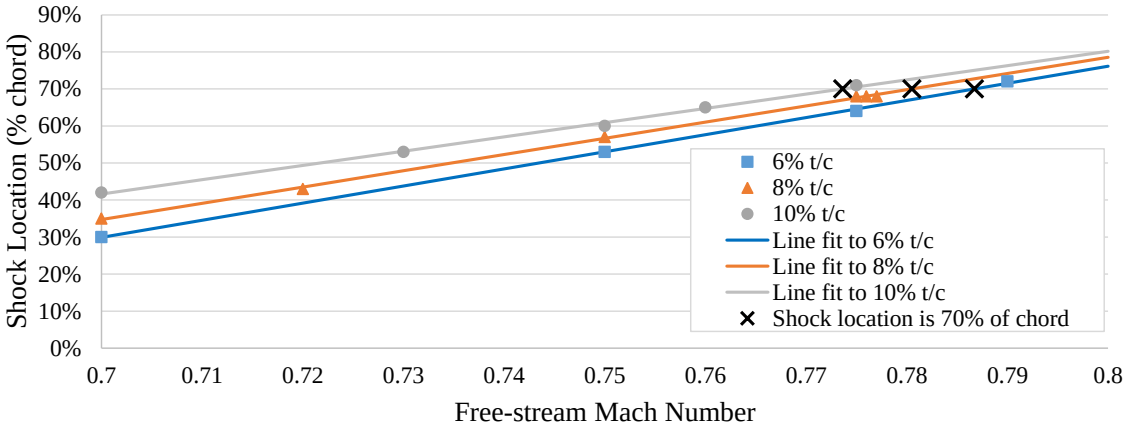

Figure 3.5: Shock location vs free-stream Mach number for a BACJ airfoil

Straight lines are fit to the data shown in figure 3.5 to determine the free-stream Mach number which will cause the shock to be at 70% of the chord. A separate line is drawn for each thickness-to-chord ratio. These three points are used to predict the free-stream Mach number at which the shock location will be 70% of the chord as a function of thickness-to-chord ratio. A straight line with a slope of -0.3275 and a y-intersection of 0.8065 was found to fit these points well. This is shown in figure 3.6. Note that the axes do not begin at zero. The free-stream Mach number at which the shock location is 70% of the chord varies from 0.787 for a thickness-to-chord ratio of 6% and to 0.774 for a thickness-to-chord ratio of 10%.

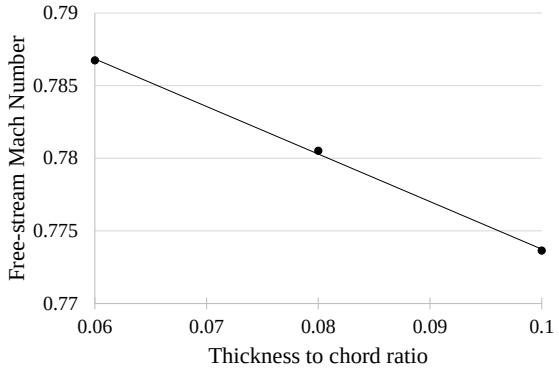

Figure 3.6: Free-stream Mach number at which shock is at 70% of chord as a function of thickness-to-chord ratio for a BACJ airfoil

The maximum allowable lift coefficient before violating the buffet constraint is shown in figure 3.7. The lift coefficient before buffet is found using the neural network shown in figure 3.4. This lift coefficient is divided by 1.3 to ensure that there will be no buffet experienced if the lift coefficient is increased by 1.3. If the free-stream Mach number is higher than the Mach number at which the shock is at 70% of the chord, shown in figure 3.6, this model is not used and the maximum allowable lift coefficient is taken as whatever was set by the MDO user, usually 0.7 or 0.8.

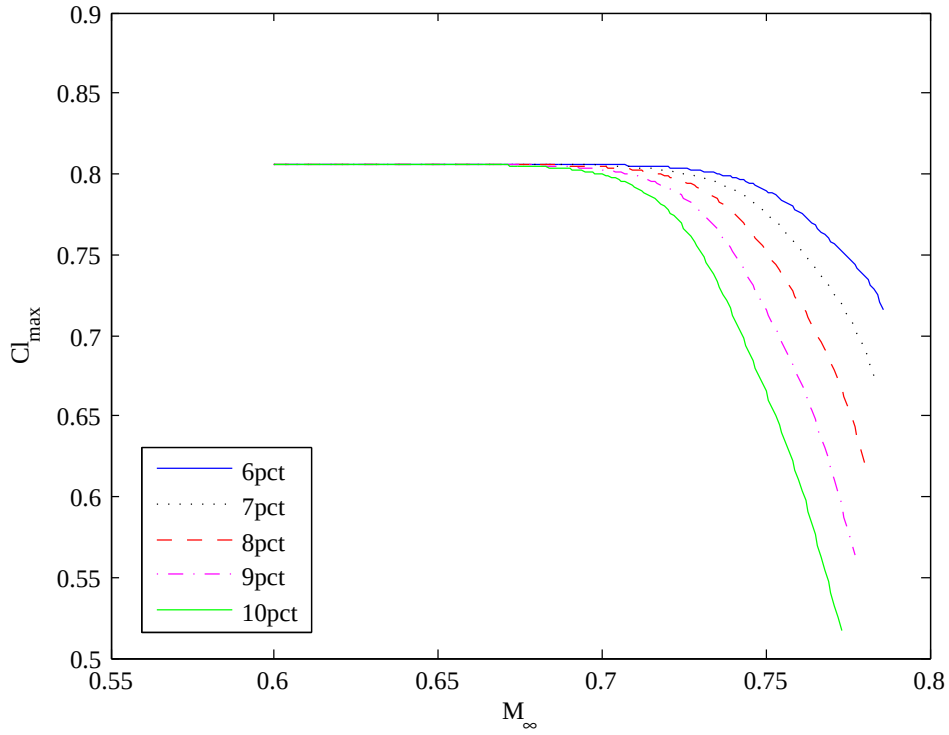

Figure 3.7: Maximum lift coefficient before buffet for a BACJ airfoil

3.3 Implementation in MDO Code

The model for the maximum allowable lift coefficient before buffet has been implemented in the 'AeroCalc' section of the MDO code. The function 'FindMaximum2DCl,' which is where the maximum 2D lift coefficient constraint is evaluated, was modified. For each wing strip, the maximum allowable lift coefficient before buffet is evaluated from the thickness-to-chord ratio and the free-stream Mach number, both modified for wing sweep using equations 1.6 and 1.7.

If the maximum allowable lift coefficient before buffet is higher than the maximum lift coefficient allowed by the user, or if the shock location is greater than 70% of the chord, then the maximum allowable lift coefficient is taken to be the one set by the MDO user. The actual two-dimensional lift coefficient for the wing strip is found using equation 1.4.

The maximum lift coefficient constraint is evaluated using equation 3.3. This will be greater than 0 if the constraint is violated and less than 0 if the constraint is not violated. The higher the value of this constraint, the more the constraint is violated.

$$\text{Con}_{Cl_{max}} = \frac{|C_l|}{C_{l,max}} - 1 \tag{3.3}$$

This constraint is evaluated at each wing strip. The highest value is taken to be the final value for this constraint.

Chapter 4

Wave Drag Model

The CFD results used to create the database assumed the flow was all turbulent. This could have a significant effect on the skin friction drag predicted by the CFD results. The current method used by the MDO, which is described in the Introduction, does consider the effect of laminar-turbulent transition based on empirical results including technology factors, and should produce more accurate predictions for skin friction drag than the CFD results. For this reason, the CFD results are only used to calculate wave drag. Skin friction drag is still calculated using the previous empirical method.

4.1 Model Description

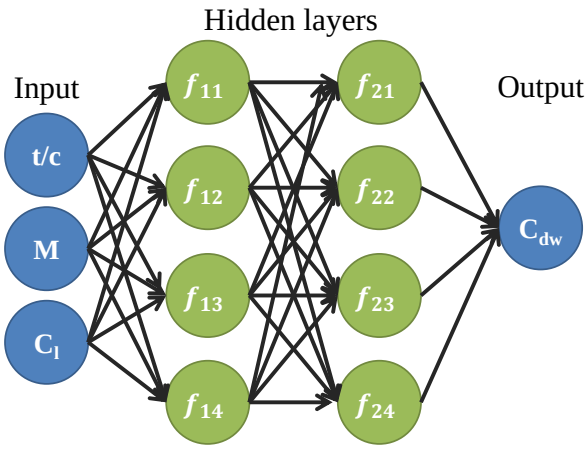

Figure 4.1: Diagram of neural network for BACJ wave drag coefficient

The CFD results for the wave drag coefficient were used to train a neural network, which then acts as a surrogate model. A neural network with two layers of four nodes was used. Using more nodes than this was not found to improve the fit of the model significantly. A diagram of this model is shown in figure 4.1. The inputs for the model are thickness-to-chord ratio, free-stream Mach number, and lift coefficient. Hyperbolic tangent functions are used as the activation functions for each node. This is shown in equations 4.1 and 4.2.

$$f_{1,i} = \tanh\left(\frac{1}{2}\left(w_{1,i,0} + w_{1,i,1}\frac{t}{c} + w_{1,i,2}M + w_{1,i,3}C_l\right)\right) \tag{4.1}$$

$$f_{2,i} = \tanh\left(\frac{1}{2}\left(w_{2,i,0} + \sum_{j=1}^{4} w_{2,i,j}f_{1,j}\right)\right) \tag{4.2}$$

The output from the neural network is determined with equation 4.3

$$C_{dw} = w_{3,0} + \sum_{i=1}^{4} w_{3,i}f_{2,i} \tag{4.3}$$

The weights for the neural network are listed in table 4.1.

Table 4.1: Wave drag coefficient neural network weights

(a) First layer

$w_{1,1,0}$	-16.57592805
$w_{1,1,1}$	-14.81411074
$w_{1,1,2}$	19.80349671
$w_{1,1,3}$	-1.19052164
$w_{1,2,0}$	-2.08498594
$w_{1,2,1}$	2.18887186
$w_{1,2,2}$	2.16025342
$w_{1,2,3}$	-0.75809659
$w_{1,3,0}$	25.39618521
$w_{1,3,1}$	-29.02907282
$w_{1,3,2}$	-25.44126098
$w_{1,3,3}$	-0.86377069
$w_{1,4,0}$	23.84912552
$w_{1,4,1}$	-33.23389355
$w_{1,4,2}$	-23.18646344
$w_{1,4,3}$	-1.65261352

(b) Second layer

$w_{2,1,0}$	-2.30952424
$w_{2,1,1}$	-2.02568889
$w_{2,1,2}$	0.29448860
$w_{2,1,3}$	-5.84918420
$w_{2,1,4}$	4.24871797
$w_{2,2,0}$	-2.14874256
$w_{2,2,1}$	0.04816940
$w_{2,2,2}$	2.57261364
$w_{2,2,3}$	0.14052278
$w_{2,2,4}$	0.32331801
$w_{2,3,0}$	-1.68477649
$w_{2,3,1}$	-1.63314701
$w_{2,3,2}$	1.35659967
$w_{2,3,3}$	0.02078852
$w_{2,3,4}$	-0.57329822
$w_{2,4,0}$	2.84367474
$w_{2,4,1}$	-0.21879128
$w_{2,4,2}$	1.54611408
$w_{2,4,3}$	-2.31414159
$w_{2,4,4}$	2.62200143

(c) Output

$w_{3,0}$	1.24744772
$w_{3,1}$	0.35443661
$w_{3,2}$	0.41644307
$w_{3,3}$	-0.14559366
$w_{3,4}$	-0.76998533

Figure 4.2 compares the neural network results and the original CFD wave drag results for each of the three thickness-to-chord ratios. The neural network matches the original data closely. The neural network has an R^2 value of 0.9977 and a root-mean-squared error of 0.0021.

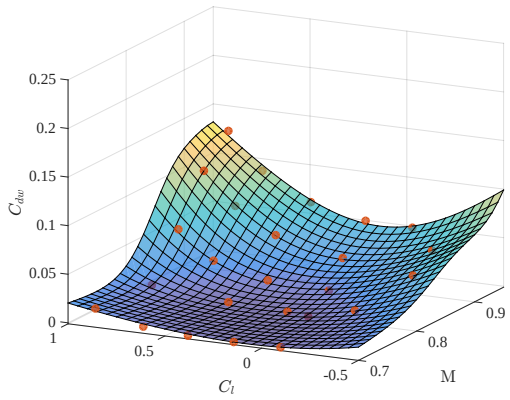

(a) Thickness to chord ratio of 6%

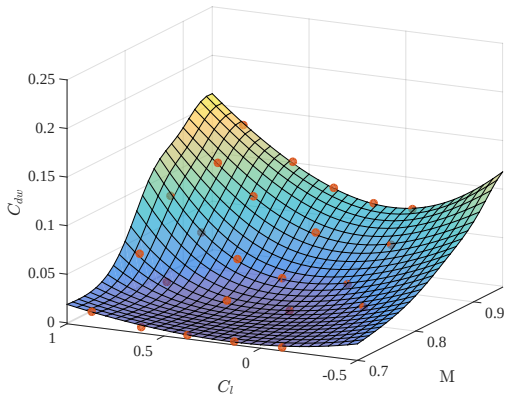

(b) Thickness to chord ratio of 8%

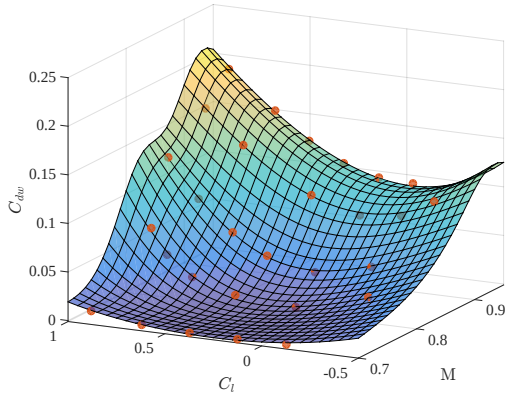

(c) Thickness to chord ratio of 10%

Figure 4.2: BACJ airfoil wave drag coefficient vs. lift coefficient for free-stream Mach numbers from 0.7 to 0.95

4.2 Comparison to validation results

The neural network predictions for wave drag are compared to the validation results for wave drag in figure 4.3. These validation results were found using SU2 with the same method as the original CFD results, however they were not used to train the neural network. There is good agreement between the validation results and the neural network model. The root-

mean-squared error between the results is 1.5×10^{-3}.

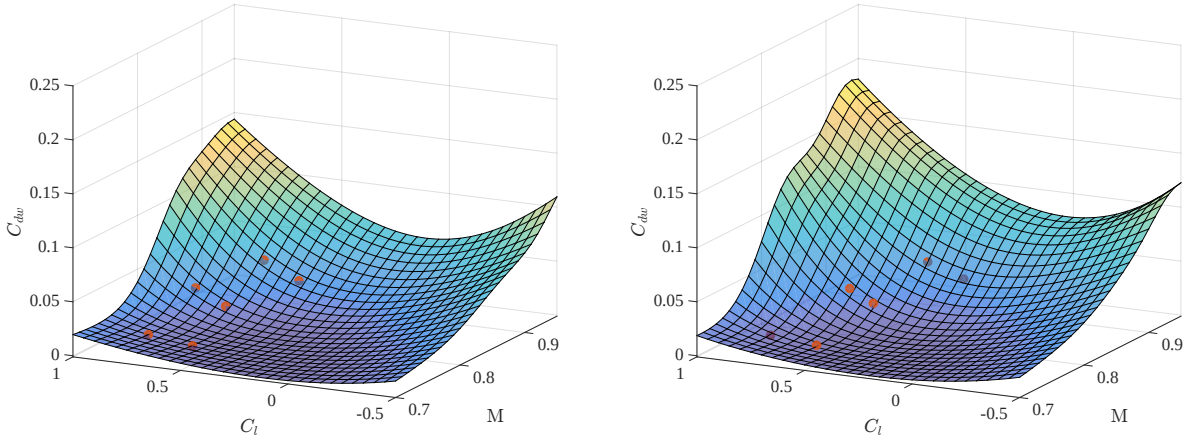

(a) Thickness to chord ratio of 7%

(b) Thickness to chord ratio of 9%

Figure 4.3: BACJ airfoil wave drag coefficient vs. lift coefficient for free-stream Mach numbers from 0.7 to 0.95

4.3 Implementation in MDO Code

The function 'wdragsubcall.f' was modified to incorporate this model. A flag, database_flag, was added to allow the user to choose whether to calculate wave drag using the original method or to calculate wave drag using the new model described here. If database_flag is set to 1, the function will use this new model to find the wave drag. If it is set to 0, the function will use the original method to calculate wave drag.

First, sweep theory is used to find the two-dimensional lift coefficient, thickness-to-chord ratio, and free-stream Mach number for each wing strip using equations 1.6, 1.7, and 1.4. If the two-dimensional free-stream Mach number is greater than or equal to 0.7, then they are used as the input for the neural network described in the above section to find the two-dimensional wave drag coefficient for the wing strip. This value is adjusted for sweep angle using equation 1.5.

If the two-dimensional free-stream Mach number is less than or equal to 0.6, the original method with the Korn equation and Lock's fourth power law is used to find the two-dimensional wave drag. This requires a Korn technology factor to be chosen. This is a function of the airfoil shape, and should be independent of the thickness-to-chord ratio and free-stream Mach number. The Korn technology factor found for the BACJ airfoil shape is 0.875635. This is found from the CFD wave drag results. The Korn factor for a particular point from the CFD database can be found by solving equations 1.8, 1.9, and 1.11 for the Korn factor. With the restriction that the Korn factor must be between 0 and 1, this results in the following equation.

$$\kappa_a = \frac{1}{10}\left(-\sqrt{2}5^{3/4}C_{dw}^{1/4} + 10\left(M + t/c + \frac{C_l}{10} + \left(\frac{.1}{80}\right)^{1/3}\right)\right) \tag{4.4}$$

Equation 4.4 is used to find the Korn factor for the BACJ airfoil at each point in the CFD database. The mean of these results is used as the Korn factor for the BACJ airfoil.

The region where the two-dimensional free-stream Mach number is between 0.6 and 0.7 transitions between the two methods. When the free-stream Mach number is 0.6, the Korn equation and Lock's fourth power law method is used to find the wave drag. When the free-stream Mach number is 0.7, the neural network is used to find the wave drag. When the free-stream Mach number is 0.65, and average of the two methods is used. This is shown in equation 4.5, where $C_{DW,Korn}$ is the wave drag coefficient found using the Korn equation and Lock's fourth power law, and $C_{DW,DB}$ is the wave drag coefficient found using the neural network model.

$$C_{DW} = \frac{1}{10}(0.7 - M_{2D})C_{DW,Korn} + (1 - \frac{1}{10}(0.7 - M_{2D}))C_{DW,DB} \tag{4.5}$$

Chapter 5

Center of Pressure Location Model

5.1 Model Description

The center of pressure is the point at which the moment on the airfoil is zero. For low angles of attack, when the lift and the force normal to the chord are approximately equal, the chordwise center of pressure location is related to the lift and quarter chord moment coefficient by the following expression:

$$\bar{x}_{cp} = -\frac{C_m}{C_l} + \frac{1}{4} \tag{5.1}$$

The CFD results for the center of pressure location are shown in figure 5.1. Only the cases with positive lift and center of pressure locations less than 140% of chord are shown. Note that the center of pressure moves aft as the free-stream Mach number is increased until a free-stream Mach number of 0.9. When the free-stream Mach number is increased beyond 0.9, the center of pressure begins to move forward again. It can be seen that the center of pressure location is strongly dependent on lift. This is because the BACJ airfoil is cambered, and the moment is not zero when the lift is zero. This causes the center of pressure to have a discontinuity when the lift is zero [39].

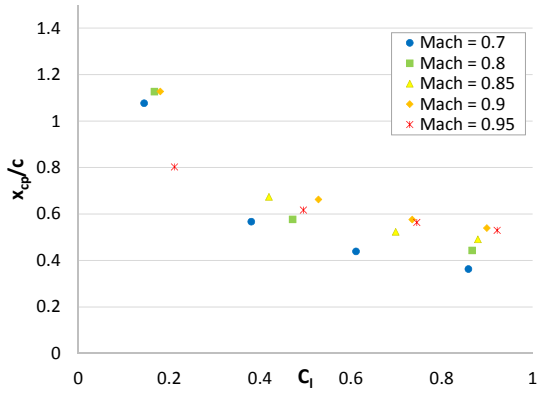

(a) thickness-to-chord ratio of 6%

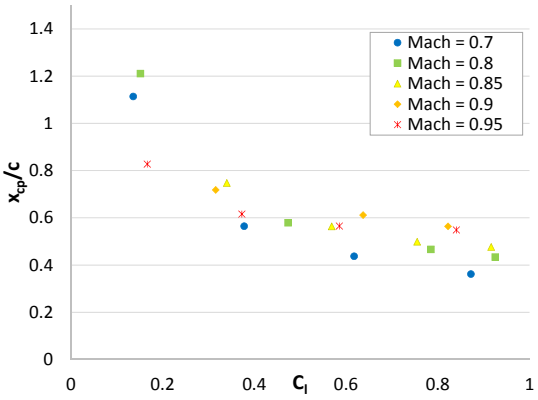

(b) Thickness to chord ratio of 8%

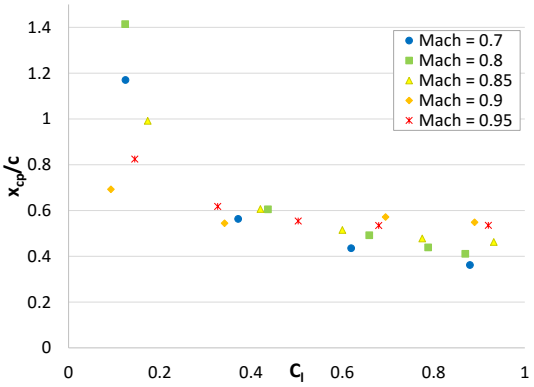

(c) Thickness to chord ratio of 10%

Figure 5.1: BACJ center of pressure location vs. lift coefficient for free-stream Mach numbers from 0.7 to 0.95

The discontinuity in the center of pressure location when the lift coefficient is zero makes it difficult to fit a surrogate model to the results. For this reason, a model is fit to the moment coefficient results, which do not have this discontinuity. By using equation 5.1, the center of pressure can be found from the moment and lift coefficient.

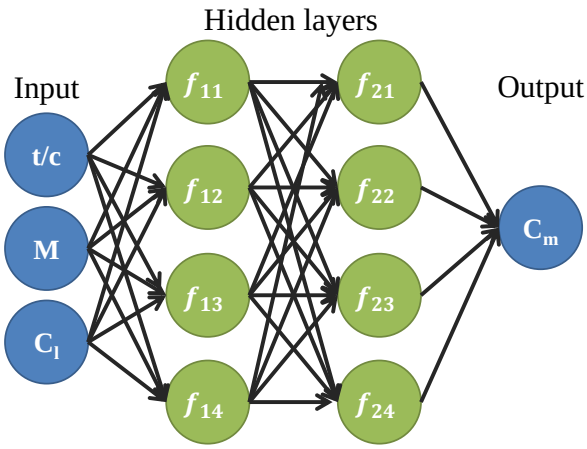

Figure 5.2: Diagram of neural network for BACJ moment coefficient

A neural network with two layers of four nodes was used as a surrogate model for the moment coefficient. Using a larger number of nodes was not found to significantly improve the fit of the model. A diagram of the neural network used is shown in figure 5.2. Hyperbolic tangent functions are used for the activation functions of each node. These are shown in equations 5.2 and 5.3.

$$f_{1,i} = \tanh\left(\frac{1}{2}\left(w_{1,i,0} + w_{1,i,1}\frac{t}{c} + w_{1,i,2}M + w_{1,i,3}C_l\right)\right) \tag{5.2}$$

$$f_{2,i} = \tanh\left(\frac{1}{2}\left(w_{2,i,0} + \sum_{j=1}^{4} w_{2,i,j}f_{1,j}\right)\right) \tag{5.3}$$

The output from the neural network is the quarter chord moment coefficient. This is determined with equation 5.4

$$C_m = w_{3,0} + \sum_{i=1}^{4} w_{3,i}f_{2,i} \tag{5.4}$$

The weights for the neural network are given in table 5.1 a-c. This model has an R^2 value of 0.9916 and an root mean squared error of 0.0057.

Table 5.1: Moment coefficient neural network weights

(a) First layer

$w_{1,1,0}$	21.894853
$w_{1,1,1}$	-33.963640
$w_{1,1,2}$	-22.118623
$w_{1,1,3}$	2.450325
$w_{1,2,0}$	-6.244297
$w_{1,2,1}$	34.644925
$w_{1,2,2}$	3.197771
$w_{1,2,3}$	1.270932
$w_{1,3,0}$	-21.089754
$w_{1,3,1}$	-37.880602
$w_{1,3,2}$	26.893185
$w_{1,3,3}$	2.491252
$w_{1,4,0}$	-15.654553
$w_{1,4,1}$	28.851562
$w_{1,4,2}$	16.702562
$w_{1,4,3}$	0.627631

(b) Second layer

$w_{2,1,0}$	-0.007435
$w_{2,1,1}$	-1.760941
$w_{2,1,2}$	0.086416
$w_{2,1,3}$	0.596684
$w_{2,1,4}$	-0.896296
$w_{2,2,0}$	-0.006884
$w_{2,2,1}$	-0.142737
$w_{2,2,2}$	1.453467
$w_{2,2,3}$	0.904119
$w_{2,2,4}$	-0.215974
$w_{2,3,0}$	-0.641619
$w_{2,3,1}$	-0.629563
$w_{2,3,2}$	0.980391
$w_{2,3,3}$	1.021283
$w_{2,3,4}$	-0.551858
$w_{2,4,0}$	0.140912
$w_{2,4,1}$	0.469687
$w_{2,4,2}$	0.686537
$w_{2,4,3}$	0.116715
$w_{2,4,4}$	-0.778198

(c) Output

$w_{3,0}$	-0.256947
$w_{3,1}$	0.423188
$w_{3,2}$	0.246651
$w_{3,3}$	-0.663750
$w_{3,4}$	0.158971

Figure 5.3 compares the surrogate model results for moment coefficient to the CFD results. The CFD results are shown with orange spheres. The model appears to behave well between the known values for the moment coefficient. The trends in the moment coefficient are clearer in this figure than they were in figure 2.10. The moment coefficient does not vary much

with lift coefficient at lower free-stream Mach numbers. As the free-stream Mach number increases, the moment coefficient begins to increase as the lift coefficient is increased. This happens sooner at higher lift coefficients and higher thickness-to-chord ratios. It is likely that this increase in the slope of the moment coefficient with respect to the lift coefficient is caused by the appearance of shocks in the flow, which appear sooner at higher lift coefficients and higher thickness-to-chord ratios. For the 10% thickness-to-chord ratio case, the variation of the moment coefficient with the lift coefficient becomes almost linear when the free-stream Mach number is 0.95. At this point, the shocks are near the trailing edge of the airfoil, and their location does not change much as the lift coefficient is varied. The slope of the moment coefficient with respect to the lift coefficient for the 8% and 6% thickness-to-chord ratio airfoils is beginning to become constant when the free-stream Mach number is 0.95. It is likely that if the free-stream Mach number were increased further, these would become almost linear as well.

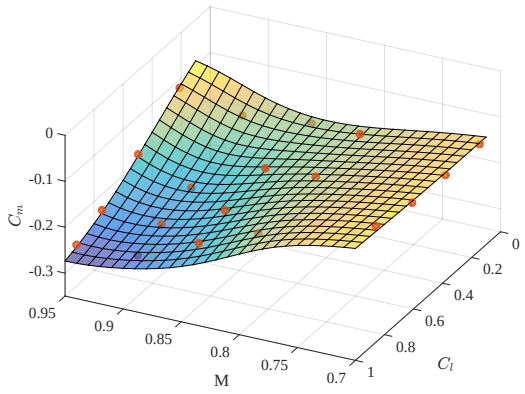

(a) thickness-to-chord ratio of 6%

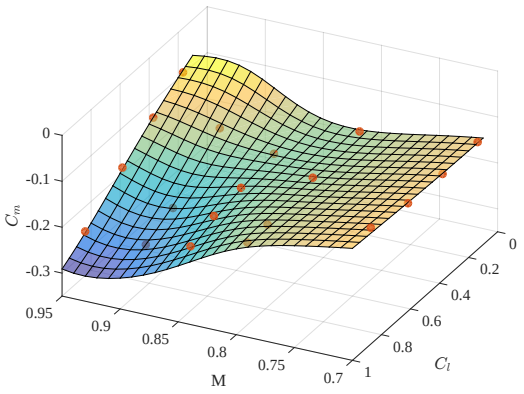

(b) Thickness to chord ratio of 8%

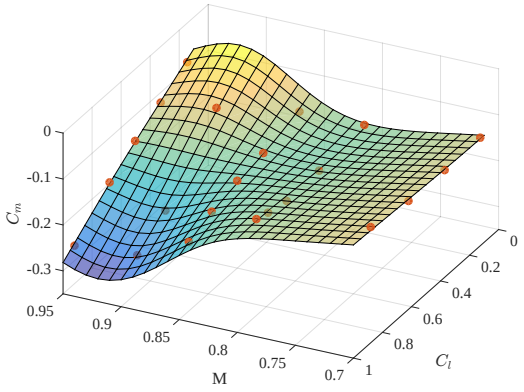

(c) Thickness to chord ratio of 10%

Figure 5.3: Surrogate model for quarter chord moment coefficient for BACJ airfoil

The center of pressure location can be found from the lift and quarter-chord moment coefficients using equation 5.1. Figure 5.4 shows the center of pressure location as a function of lift coefficient and free-stream Mach number using the moment coefficients predicted by the surrogate model. Results are shown for three thickness-to-chord ratios. The CFD results are shown with orange spheres. Only cases with lift coefficients greater than 0.1 are shown. The model has an R^2 value of 0.9988. The root-mean-squared error is 0.2972, which is somewhat high. However, if only points with lift coefficients greater than 0.05 are considered, the root mean squared error is reduced to 0.0278. If the minimum lift coefficient is increased to 0.2,

the root-mean-squared error is reduced further to 0.0087. The majority of the error between the CFD results and the model is at points with very low lift coefficients, where the center of pressure location changes rapidly. At higher lift coefficients, this model has good agreement with the CFD results.

For the 10% thickness-to-chord ratio airfoil at a low coefficient of lift, there is a large dip in the center of pressure location when the free-stream Mach number is 0.9. This can be explained by figure 5.3, where it can be seen that the moment coefficient is nearly zero when the lift is zero. The low moment coefficient at this location keeps the center of pressure location from increasing as rapidly as the lift coefficient goes to zero. A similar trend can be seen for the 8% thickness-to-chord ratio airfoil, although the dip is not as pronounced.

Another interesting trend in the center of pressure location is that at high lift coefficients, the center of pressure location moves aft as the free-stream Mach number is increased. This agrees with the trends from reference [20].

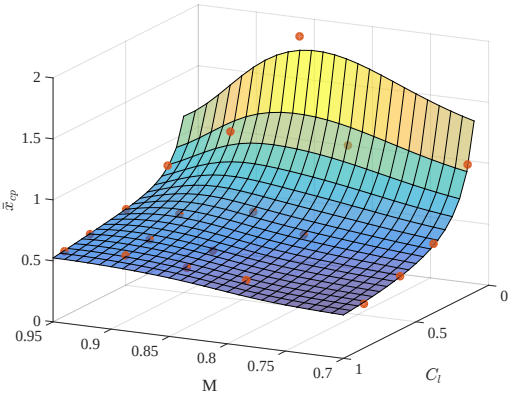

(a) thickness-to-chord ratio of 6%

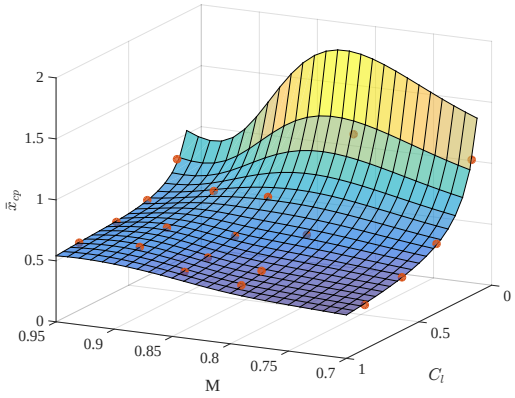

(b) Thickness to chord ratio of 8%

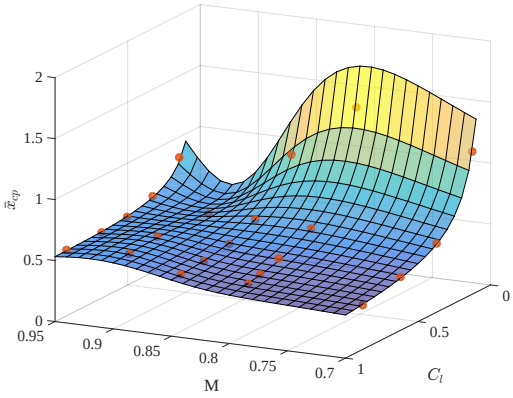

(c) Thickness to chord ratio of 10%

Figure 5.4: Surrogate model for center of pressure location for BACJ airfoil

5.2 Comparison to validation results

The center of pressure location results from the validation runs are compared to the surrogate model in figure 5.5. The root-mean-squared error between the validation results and the surrogate model is 0.0172.

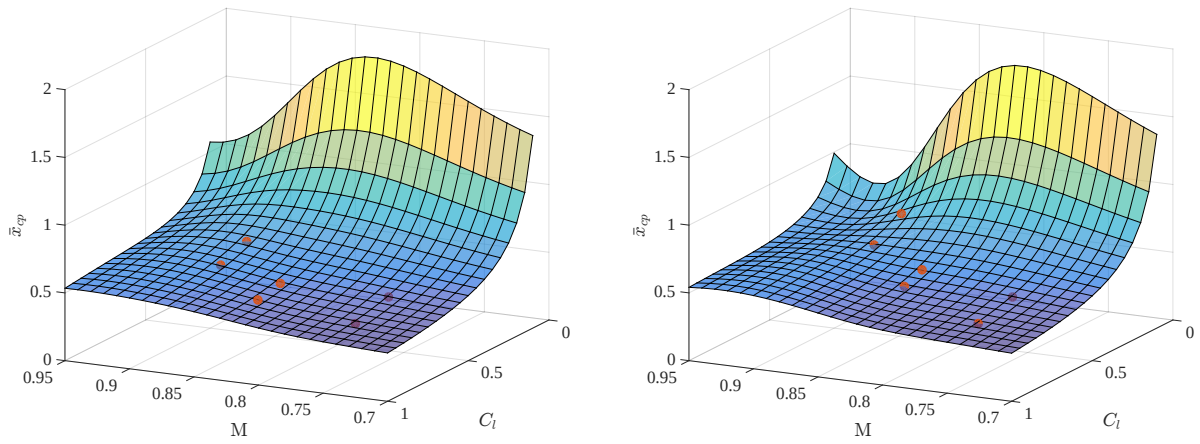

(a) Thickness to chord ratio of 7%

(b) Thickness to chord ratio of 9%

Figure 5.5: BACJ airfoil center of pressure location vs. lift coefficient and free-stream Mach number

5.3 Implementation in MDO Code

A function to find the center of pressure location was written and added to the MDO code. This function takes the lift coefficient, thickness-to-chord ratio, free-stream Mach number, and sweep angle for a single wing strip as inputs. It returns the center of pressure location.

To find the center of pressure location, the lift coefficient, thickness-to-chord ratio, and free-stream Mach number are first corrected for wing sweep using equations 1.6, 1.7, and 1.4. These two-dimensional values are used as the input for the neural network model for the moment coefficient. Once the moment coefficient is known, the center of pressure location can be found using equation 5.1.

Chapter 6

Lift Curve Slope Model

6.1 Model Description

To find the lift curve slope, a surrogate model was fit to the CFD results to relate lift coefficient to thickness-to-chord ratio, free-stream Mach number, and angle of attack. By finding derivatives of this model with respect to angle of attack, the lift curve slope can be determined. Because the MDO will find the lift curve slope as a function of lift coefficient, rather than angle of attack, a second model was created to find angle of attack as a function of thickness-to-chord ratio, free-stream Mach number, and lift coefficient.

6.1.1 Model for lift coefficient

The first model used to find the lift curve slope relates the lift coefficient to the thickness-to-chord ratio, the free-stream Mach number, and the angle of attack. A neural network with one layer of ten nodes is used. This was found to be enough nodes to match the data well. A single hidden layer was used to make it easier to find derivatives of this model. A diagram of this neural network is shown in figure 6.1.

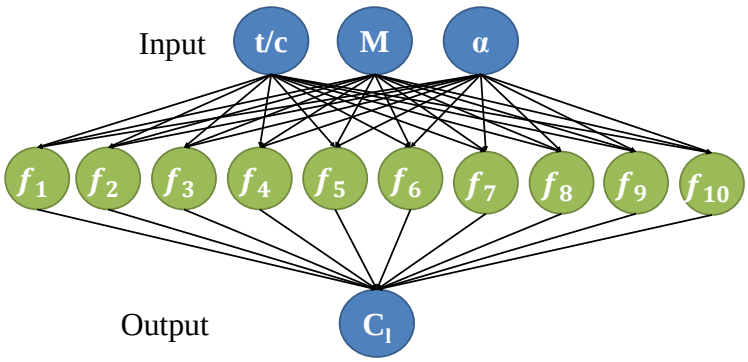

Figure 6.1: Diagram of neural network for BACJ lift coefficient

Hyperbolic tangent functions are used as the activation functions in the hidden layer. This is shown in equation 6.1.

$$f_i = \tanh\left(\frac{1}{2}\left(w_{1,i,0} + w_{1,i,1}\frac{t}{c} + w_{1,i,2}M + w_{1,i,3}\alpha\right)\right) \tag{6.1}$$

The output is given by equation 6.2.

$$C_l = w_{2,0} + \sum_{i=1}^{10} w_{2,i} f_i \tag{6.2}$$

The weights for this neural network are listed in table 6.1.

Table 6.1: Lift coefficient neural network weights

(a) Input layer, nodes 1-5

$w_{1,1,0}$	72.35241003
$w_{1,1,1}$	-102.6315491
$w_{1,1,2}$	-73.01497095
$w_{1,1,3}$	1.03974911
$w_{1,2,0}$	7.481012209
$w_{1,2,1}$	20.53520505
$w_{1,2,2}$	-10.11844122
$w_{1,2,3}$	-0.187769206
$w_{1,3,0}$	11.06281649
$w_{1,3,1}$	55.81528224
$w_{1,3,2}$	-18.73836982
$w_{1,3,3}$	-0.008760951
$w_{1,4,0}$	-3.275989852
$w_{1,4,1}$	-19.7982111
$w_{1,4,2}$	4.798023058
$w_{1,4,3}$	-0.148800761
$w_{1,5,0}$	-43.47737748
$w_{1,5,1}$	7.93685317
$w_{1,5,2}$	50.25939537
$w_{1,5,3}$	0.707508053

(b) Input layer, nodes 6-10

$w_{1,6,0}$	-18.96613142
$w_{1,6,1}$	-17.61962038
$w_{1,6,2}$	23.52420742
$w_{1,6,3}$	0.111768873
$w_{1,7,0}$	3.200470518
$w_{1,7,1}$	-6.562269776
$w_{1,7,2}$	-6.354551664
$w_{1,7,3}$	-0.554760186
$w_{1,8,0}$	-19.76651495
$w_{1,8,1}$	40.9595194
$w_{1,8,2}$	20.98238278
$w_{1,8,3}$	0.713240333
$w_{1,9,0}$	-14.91358343
$w_{1,9,1}$	42.68799105
$w_{1,9,2}$	15.32149666
$w_{1,9,3}$	-0.209530226
$w_{1,10,0}$	-1.723002634
$w_{1,10,1}$	-15.51708395
$w_{1,10,2}$	2.325361165
$w_{1,10,3}$	0.123914955

(c) Output layer

$w_{2,0}$	-0.443547853
$w_{2,1}$	0.205702956
$w_{2,2}$	-1.551036801
$w_{2,3}$	-0.020160322
$w_{2,4}$	-0.673324412
$w_{2,5}$	-0.183925396
$w_{2,6}$	-0.35929491
$w_{2,7}$	-0.305312106
$w_{2,8}$	0.242245539
$w_{2,9}$	-0.382453928
$w_{2,10}$	-1.177081586

The model used for the lift coefficient is shown in figure 6.2 for three thickness-to-chord ratios. The points found using CFD are shown with orange spheres. This model has an R^2 value of 0.9986 and an root mean squared error of 0.0138, so it fits the CFD data closely. There seem to be three regions in the lift coefficient results. At low free-stream Mach numbers and

moderate angles of attack, the lift coefficient varies linearly with angle of attack. For higher angles of attack and free-stream Mach numbers between 0.8 and 0.9, there is a second region where the change in lift coefficient with angle of attack also appears linear, but with a much lower slope than the first region. The third region occurs at high Mach numbers and low angles of attack. The lift coefficient appears to behave linearly in this region as well, and has a slope similar to the first region. However, there is a significant and sudden drop in lift coefficient when moving from the first or the second region to this third region.

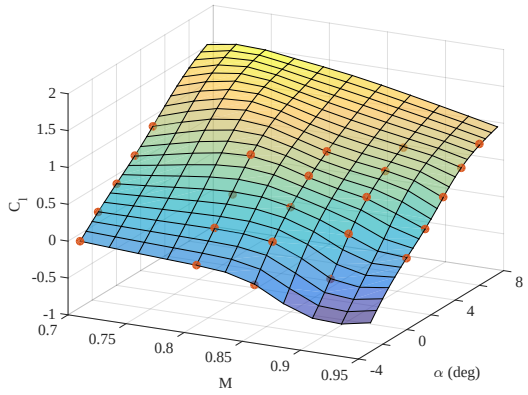

(a) thickness-to-chord ratio of 6%

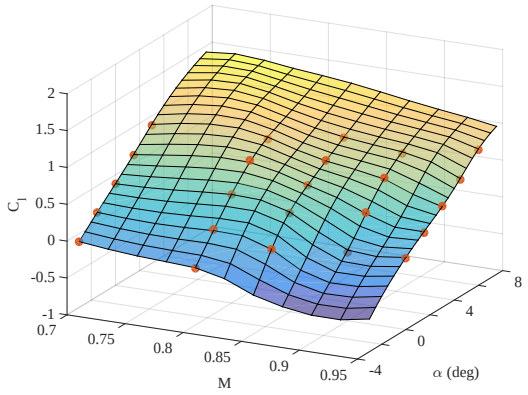

(b) Thickness to chord ratio of 8%

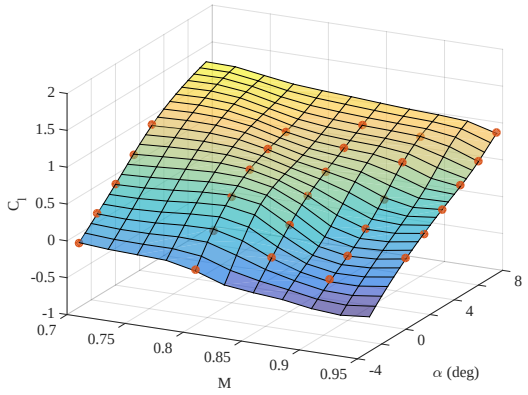

(c) Thickness to chord ratio of 10%

Figure 6.2: Surrogate model for the lift coefficient for BACJ airfoil

The lift curve slope can be found as a function of thickness-to-chord ratio, free-stream Mach

number, and angle of attack by taking the derivative of this model with respect to angle of attack. Taking the derivative of equation 6.2 with respect to angle of attack gives:

$$\frac{dC_l}{d\alpha} = \sum_{i=1}^{10} w_{2,i} \frac{df_i}{d\alpha} \tag{6.3}$$

where $\frac{df_i}{d\alpha}$ is given by equation 6.4 and can be found by differentiating equation 6.1 with respect to angle of attack.

$$\frac{df_i}{d\alpha} = \frac{1}{2} w_{1,i,3} \operatorname{sech}^2 \left(\frac{1}{2} \left(w_{1,i,0} + w_{1,i,1} \frac{t}{c} + w_{1,i,2} M + w_{1,i,3} \alpha \right) \right) \tag{6.4}$$

6.1.2 Derivative of lift coefficient model

The derivative of the model for lift coefficient with respect to angle of attack is shown in figure 6.3. Note that although angle of attack is given in degrees, the lift curve slope is given in terms of radians. Also note that angle of attack is decreasing into the page. The lift curve slope was also found directly from the CFD results using second-order accurate finite difference equations. These points are shown in orange. The root-mean-squared error between the CFD finite difference results and this model is 1.3320. However, when only points with lift coefficients between 0 and 0.8 are considered, the root-mean-squared error drops by more than half to 0.5793. The three regions which were visible in figure 6.2 correspond to the relatively flat portions of figure 6.3, with steep ridges between these regions.

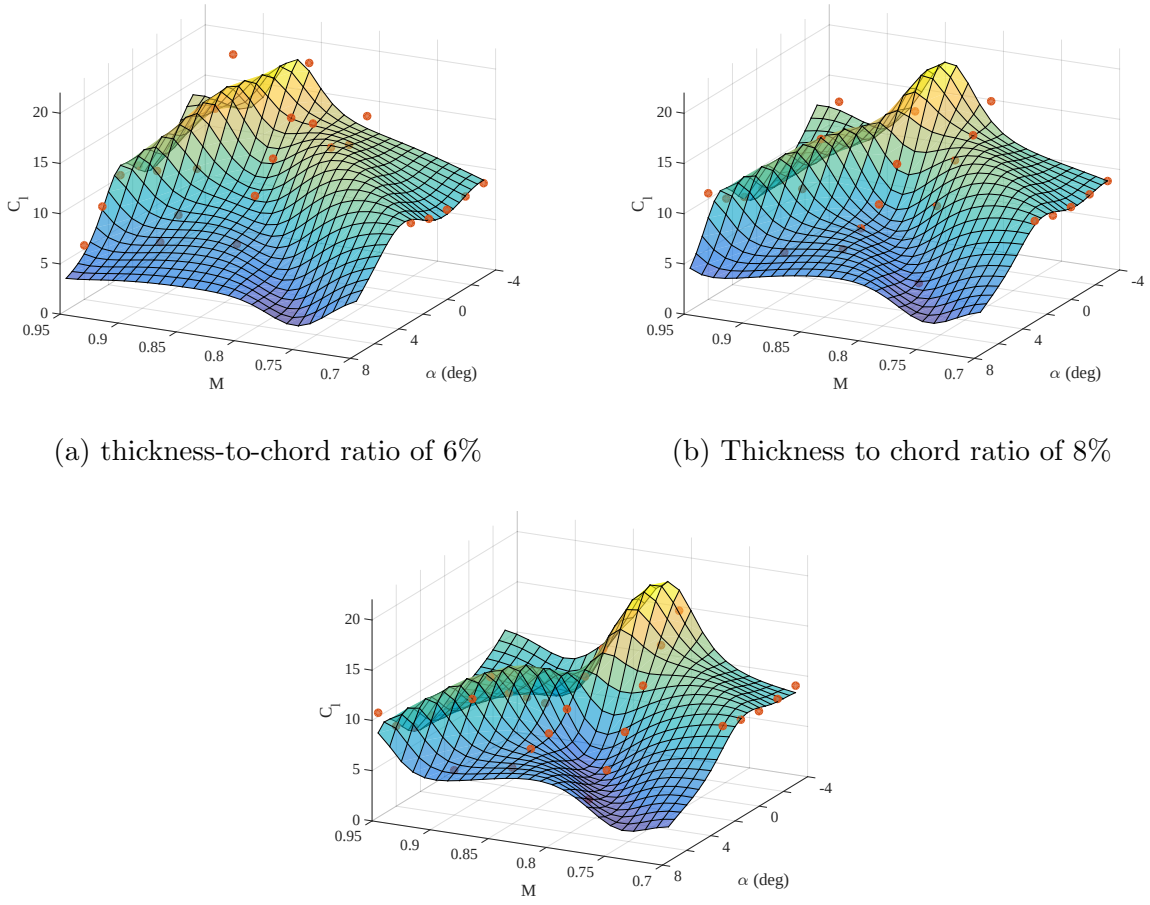

(a) thickness-to-chord ratio of 6%

(b) Thickness to chord ratio of 8%

(c) Thickness to chord ratio of 10%

Figure 6.3: Lift curve slope of BACJ airfoil as a function of free-stream Mach number and angle of attack for three thickness-to-chord ratios

6.1.3 Model for angle of attack

The lift curve slope has been found as a function of thickness-to-chord ratio, free-stream Mach number, and angle of attack. However, the angle of attack for each wing strip is not known by the MDO. As a result, it is necessary to find lift curve slope as a function of thickness-to-chord ratio, free-stream Mach number, and lift coefficient instead. For this purpose, a second model was created which gives angle of attack as a function of thickness-

to-chord ratio, free-stream Mach number, and lift coefficient. The angle of attack found using this model can then be used with the model for lift curve slope.

A neural network with one layer of ten nodes is used as a model. This was found to be enough nodes to fit the data closely enough to have almost no effect on the accuracy of the combined model. The structure of this model is similar to the model used for the lift coefficient, a diagram of which is shown in figure 6.1. The activation functions for the hidden layer are given in equation 6.5.

$$f_i = \tanh\left(\frac{1}{2}\left(w_{1,i,0} + w_{1,i,1}\frac{t}{c} + w_{1,i,2}M + w_{1,i,3}C_l\right)\right) \tag{6.5}$$

The equation for the output is the same as is shown in equation 6.2. The weights for this neural network are shown in table 6.2.

Table 6.2: Angle of attack neural network weights

(a) Input layer, nodes 1-5

$w_{1,1,0}$	30.88259441
$w_{1,1,1}$	-55.45935863
$w_{1,1,2}$	-27.43508411
$w_{1,1,3}$	-5.039254145
$w_{1,2,0}$	-1.316627694
$w_{1,2,1}$	-5.749500596
$w_{1,2,2}$	3.56194283
$w_{1,2,3}$	-3.674953901
$w_{1,3,0}$	42.3540543
$w_{1,3,1}$	-57.56387056
$w_{1,3,2}$	-43.2200332
$w_{1,3,3}$	5.129633873
$w_{1,4,0}$	-24.71044329
$w_{1,4,1}$	22.87782264
$w_{1,4,2}$	29.42254989
$w_{1,4,3}$	-3.593954575
$w_{1,5,0}$	-77.50572984
$w_{1,5,1}$	32.84144342
$w_{1,5,2}$	85.45823028
$w_{1,5,3}$	6.730727444

(b) Input layer, nodes 6-10

$w_{1,6,0}$	5.54166252
$w_{1,6,1}$	-20.97837124
$w_{1,6,2}$	1.602999754
$w_{1,6,3}$	-4.597255298
$w_{1,7,0}$	28.05637888
$w_{1,7,1}$	-59.86678728
$w_{1,7,2}$	-24.02253573
$w_{1,7,3}$	-5.583410448
$w_{1,8,0}$	5.591337242
$w_{1,8,1}$	32.88416676
$w_{1,8,2}$	-7.397132895
$w_{1,8,3}$	-1.392153107
$w_{1,9,0}$	24.89047867
$w_{1,9,1}$	22.40083489
$w_{1,9,2}$	-28.77851855
$w_{1,9,3}$	-4.076351099
$w_{1,10,0}$	-13.37157149
$w_{1,10,1}$	19.94835576
$w_{1,10,2}$	11.93556697
$w_{1,10,3}$	-4.325463767

(c) Output layer

$w_{2,0}$	4.333344626
$w_{2,1}$	-4.101920104
$w_{2,2}$	-3.059939621
$w_{2,3}$	-1.621701642
$w_{2,4}$	0.693176010
$w_{2,5}$	0.853922413
$w_{2,6}$	-4.090351441
$w_{2,7}$	3.194005428
$w_{2,8}$	-1.891818434
$w_{2,9}$	1.660518483
$w_{2,10}$	-2.565512045

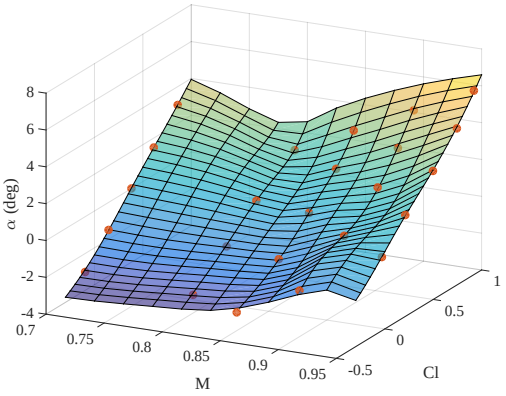

(a) thickness-to-chord ratio of 6%

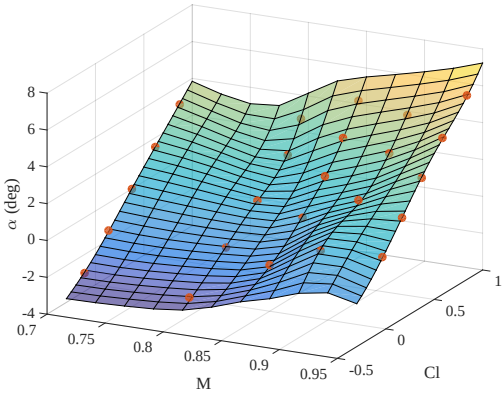

(b) Thickness to chord ratio of 8%

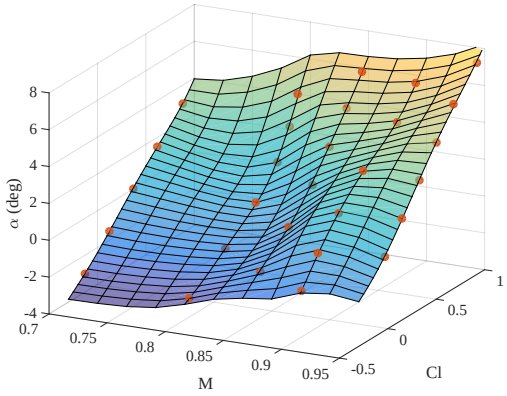

(c) Thickness to chord ratio of 10%

Figure 6.4: Lift curve slope of BACJ airfoil as a function of free-stream Mach number and lift coefficient for three thickness-to-chord ratios

6.1.4 Combined model for lift curve slope

Lift curve slope can be found from lift coefficient, free-stream Mach number, and thickness-to-chord ratio by first using the model described in the section 'Model for angle of attack' to find the angle of attack. That angle of attack can then be used with the model for the lift curve slope to find the lift curve slope. Results for lift curve slope found using this method are shown in figure 6.5. The orange points show the results of using second-order accurate

finite difference equations to find the lift curve slope directly from the database results. The root-mean-squared error between the results from the combined surrogate model and the results found using finite difference equations is 1.3362. This is only 0.0042 higher than the root-mean-squared error of the lift curve slope without using the angle of attack model, which shows that the addition of a second model for angle of attack does not have a significant effect on the overall accuracy of the results.

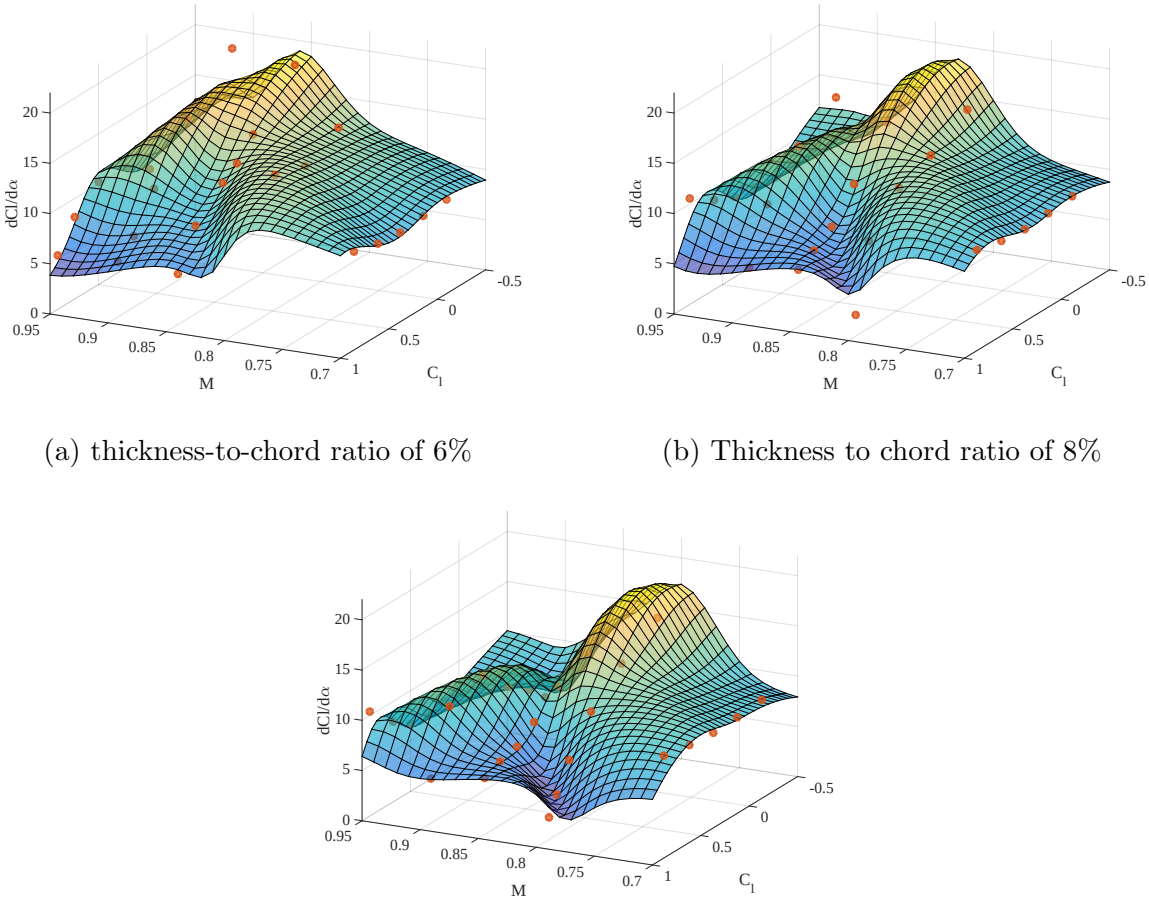

(a) thickness-to-chord ratio of 6%

(b) Thickness to chord ratio of 8%

(c) Thickness to chord ratio of 10%

Figure 6.5: Angle of attack of BACJ airfoil as a function of free-stream Mach number and lift coefficient for three thickness-to-chord ratios

It can be seen in figure 6.5 that the points where there is the largest disagreement between

the finite difference equation and the model results for lift curve slope are at either high or low lift coefficients. When only points with lift coefficients between 0 and 0.8, the range used by the MDO, are considered, the root-mean-squared error between the finite difference equation and the model results is reduced to 0.5522. Figure 6.6 shows the lift curve slope results with this limit on lift coefficient.

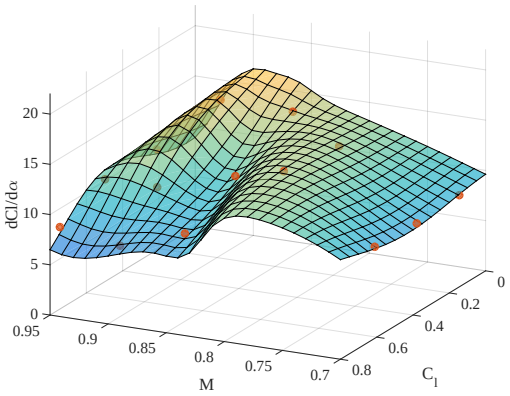

(a) thickness-to-chord ratio of 6%

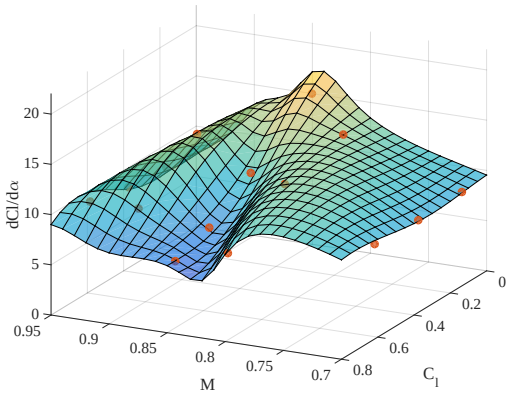

(b) Thickness to chord ratio of 8%

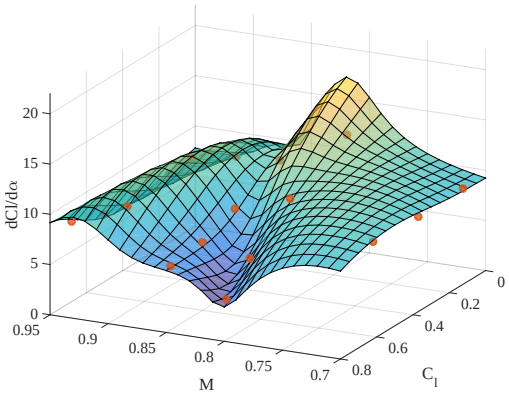

(c) Thickness to chord ratio of 10%

Figure 6.6: Angle of attack of BACJ airfoil as a function of free-stream Mach number and lift coefficient for three thickness-to-chord ratios and lift coefficients between 0 and 0.8

6.2 Comparison to validation results

The surrogate model for the lift curve slope is compared to the validation results in figure 6.7. The lift curve slope for the validation results is found using finite difference equations. Because there are only results for two points at each free-stream Mach number and thickness-to-chord ratio in the validation data, it is only possible to use first order finite difference expressions.

The root-mean-squared error between the validation results and the surrogate model is 1.4. The largest difference between the validation results and the surrogate model occurs when the thickness-to-chord ratio is 9%, the free-stream Mach number is 0.875, and the lift coefficient is 0.2841. At this location, the lift curve slope from the validation results is 9.6 while the lift curve slope from the surrogate model is 12.5, a difference of 2.9. This location is at one of the ridges in the lift curve slope for the surrogate model. The lift curve slope changes rapidly with lift coefficient and free-stream Mach number in this region. A small error in the location of this ridge could cause a large difference in the lift curve slope, and it is likely that this is what is causing the large difference between the validation results and the surrogate model at this location.

The rest of the validation results for lift curve slope have good agreement with the surrogate model. The validation results have lift curve slopes which are similar to those predicted by the surrogate model, and they show many of the same trends.

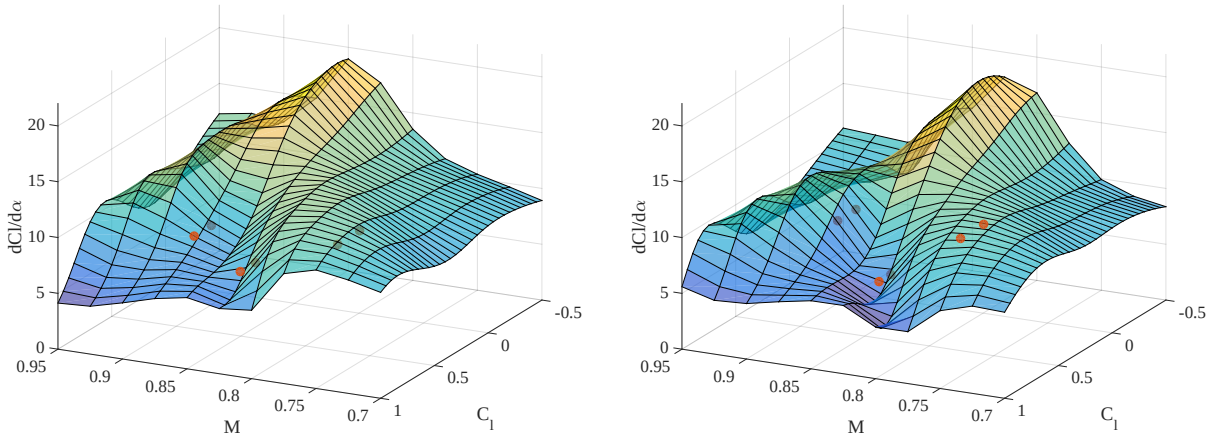

(a) Thickness to chord ratio of 7%

(b) Thickness to chord ratio of 9%

Figure 6.7: BACJ airfoil lift curve slope vs. lift coefficient and free-stream Mach number

6.3 Implementation in MDO Code

A function was created to find the lift curve slope at a given lift coefficient, thickness-to-chord ratio, free-stream Mach number, and sweep angle. First the input are adjusted for wing sweep using equations 1.6, 1.7, and 1.4. These two-dimensional values are put into the neural network to find the angle of attack. This angle of attack is used along with the two-dimensional thickness-to-chord ratio and free-stream Mach number to find the lift curve slope.

Chapter 7

Summary and Conclusion

Improvements were made to the transonic aerodynamic calculations made by the Virginia Tech MDO code to better reflect real-world physics. The presence of shocks and the mixture of subsonic and supersonic flow in the transonic regime often requires CFD to be used to obtain accurate aerodynamic results. However, as MDO requires thousands of designs to be evaluated, it would be impractical to run CFD calculations within the MDO code. Instead, a BACJ airfoil shape was chosen and two-dimensional CFD calculations were done for the range of thickness-to-chord ratios, free-stream Mach numbers, and two-dimensional lift coefficients likely to be used by the MDO. Strip theory is used within the MDO to relate these two-dimensional values to the three-dimensional wing. Steady, two-dimensional RANS equations were used with a Spalart-Allmaras turbulence model. Surrogate models were then fit to these CFD results. These surrogate models can be used by the MDO code for aerodynamic calculations. A total of four separate models were created to calculate different quantities needed by the MDO.

A set of 12 additional CFD cases were run to create a validation dataset. This dataset was used to check the accuracy of the surrogate models used in the MDO, but was not used to develop those models. The points were chosen to be at points between points used to develop the models used by the MDO.

7.1 Buffet boundary model

An empirical relationship between the onset of buffet, shock location, and the local Mach number before the shock was used to predict buffet. Several CFD calculations were done for free-stream Mach numbers between 0.7 and 0.8 until points were found which were at or just below the buffet boundary. Cases where the shock location was greater than 70% of the chord were not considered to buffet, as there was unlikely to be enough interaction with the structure to cause buffet. A neural network was fit to these points to relate the maximum allowable lift coefficient before buffet to the free-stream Mach number and the thickness-to-chord ratio. The root-mean-squared error between this model and the points used to generate it was 0.0099. This model for maximum lift coefficient before buffet was used to limit the maximum two-dimensional lift coefficient.

7.2 Wave drag model

A neural network was fit to the CFD wave drag results. This model has inputs of thickness-to-chord ratio, free-stream Mach number, and lift coefficient. The root mean squared error between the original points and the neural network results is 0.0021. The root mean squared error between the validation points and the neural network results is 0.0015.

7.3 Center of pressure model

Because the BACJ airfoil is cambered, the moment coefficient is not zero when the lift is zero. This causes the center of pressure location to have a discontinuity when the lift is zero, which makes it difficult to fit a surrogate model to the results. Instead, a neural network was fit to the moment coefficient, with inputs of thickness-to-chord ratio free-stream Mach number, and lift coefficient. The moment coefficient found from this neural network is then

used with the lift coefficient to find the center of pressure location. This model for the center of pressure was added to the aeroelastic section of the MDO code for flutter calculations.

This model has root-mean-squared error of 0.2972 when compared to the original CFD results for the center of pressure location. The majority of this error is due to points with lift coefficients near zero, as the center of pressure location changes rapidly with lift coefficient in this region. When only points with lift coefficients greater than 0.05 are considered, the root mean squared error is reduced to 0.0278. When only points with lift coefficients greater than 0.2 are considered, the root mean squared error is further reduced to 0.0087. The root mean squared error between the validation points and the model is 0.0172.

7.4 Lift curve slope model

A neural network was used to relate the lift coefficient to the thickness-to-chord ratio, free-stream Mach number, and angle of attack. The derivative of this neural network with respect to angle of attack is used to find the lift curve slope. Because this requires angle of attack as an input, which is not known by the MDO, a second neural network was used to find angle of attack as a function of thickness-to-chord ratio, free-stream Mach number, and lift coefficient. This model for the lift curve slope is used in the aeroelastic section of the MDO code for flutter calculations.

This model was compared to second-order accurate finite difference equation results for the lift curve slope found directly from the CFD data. The root mean squared error between these methods was 1.3320. It's difficult to say how much of the difference in the results is due to inaccuracies in the model and how much is due to inaccuracies in the finite difference equations. The two methods agree more closely when only points with lift coefficients between 0 and 0.8 are compared. When this is done, the root mean squared error is reduced to 0.5713.

The validation CFD results have only two points at each free-stream Mach number and

thickness-to-chord ratio, so it is only possible to use first-order accurate finite difference equations to find the lift curve slope from these points. When these results are compared to the lift curve slope model results, the root mean squared error is 1.4.

7.5 Future work

There are a number of improvements which could be made to this method for aerodynamic analysis. The effect of varying Reynolds number should be considered. All the results used for these models has been for a Reynolds number of 6×10^6. Higher Reynolds numbers tend to delay separation, while lower Reynolds numbers tend to promote separation. As many of the CFD cases run had separated flow, a change in when separation occurs could have a significant effect on the aerodynamic behavior. The effect of Reynolds number on the flow would likely be largest for free-stream Mach numbers around 0.8, when the flow is separated for higher lift coefficients and thickness-to-chord ratios but not for lower lift coefficients and thickness-to-chord ratios. At higher free-stream Mach numbers, the shocks in the flow will likely be strong enough to cause separation regardless of free-stream Mach number.

Laminar-turbulent transition could also have an impact on the flow and on separation. Laminar flow separates more easily than turbulent flow. All the results used for these models have assumed fully turbulent flow.

Obtaining results for a wider range of thickness-to-chord ratios would allow the models to be used more flexibly. The range of thickness-to-chord ratios used for these models was based on the thickness-to-chord ratios of designs from previous MDO studies. However, it is possible that future studies could have mission requirements which favored thicker or thinner wings. Adding results for thicker or thinner airfoils to the database would allow these models to be used confidently for more design applications.

Similar models could also be made for different airfoil shapes. This would allow the effect of airfoil shape on designs from the MDO to be investigated. While the BACJ airfoil is a

fairly typical supercritical airfoil, other shapes might have better performance depending on the design lift coefficient and free-stream Mach number.

Chapter 8

References

[1] Pfenninger, W., "Laminar Flow Control: Laminarization," *Special Course on Concepts for Drag Reduction*, Vol. AGARD-R-654, 1977.

[2] Meadows, N. A., Schetz, J. A., Kapania, R. K., Bhatia, M., and Seber, G., "Multidisciplinary Design Optimization of Medium-Range Transonic Truss-Braced Wing Transport Aircraft," *Journal of Aircraft*, Vol. 49, No. 6, 2012, pp. 1844–1856.

[3] Mallik, W., Kapania, R. K., and Schetz, J. A., "Effect of Flutter on the Multidisciplinary Design Optimization of Truss-Braced-Wing Aircraft," *Journal of Aircraft*, Vol. 52, No. 6, 2015, pp. 1858–1872.

[4] Seber, G., Ran, H., Schetz, J., and Mavris, D., "Multidisciplinary Design Optimization of a Truss Braced Wing Aircraft with Upgraded Aerodynamic Analyses," *29th AIAA Applied Aerodynamics Conference*, 2011, p. 3179.

[5] Obert, E., *Aerodynamic Design of Transport Aircraft*, Ios Press, 2009.

[6] Bushnell, D. M., "Fluid Mechanics, Drag Reduction and Advanced Configuration Aeronautics," Tech. Rep. NASA-TM-2000-210646, 2000.

[7] Callaghan, J. T. and Liebeck, R. H., "Some Thoughts on the Design of Subsonic Transport Aircraft for the 21st Century," Tech. Rep. No. 901987, SAE Technical Paper, 1990.

[8] Joslin, R. D., "Aircraft Laminar Flow Control 1," *Annual Review of Fluid Mechanics*, Vol. 30, No. 1, 1998, pp. 1–29.

[9] Pfenninger, W., "Design Considerations of Large Subsonic Long Range Transport Airplanes with Low Drag Boundary Layer Suction," Tech. Rep. NAI-54-800 (BLC-67), Northrop Aircraft, Inc., 1957.

[10] Kulfan, R. M. and Vachal, J. D., "Wing Planform Geometry Effects on Large Subsonic Military Transport Airplanes." Tech. rep., DTIC Document, 1978.

[11] Turriziani, R., Lovell, W., Martin, G., Price, J., Swanson, E., and Washburn, G., "Preliminary Design Characteristics of a Subsonic Business Jet Concept Employing an Aspect Ratio 25 Strut Braced Wing," Tech. Rep. 159361, NASA Contract NAS1-16000, 1980.

[12] Smith, P. M., DeYoung, J., Lovell, W. A., Price, J. E., and Washburn, G. F., "A Study of High-Altitude Manned Research Aircraft Employing Strut-Braced Wings of High-Aspect-Ratio," Tech. Rep. NASA-CR-159262, NASA Contract NASl-16000, 1981.

[13] Grasmeyer III, J. M., *Multidisciplinary Design Optimization of a Strut-Braced Wing Aircraft*, Master's thesis, Virginia Polytechnic Institute and State University, Blacksburg, VA, 1998.

[14] Gundlach, J., Tétrault, P. A., Gern, F., Nagshineh-Pour, A., Ko, A., Schetz, J., Mason, W., Kapania, R., Grossman, B., and Haftka, R., "Multidisciplinary Design Optimization of a Strut-Braced Wing Transonic Transport," *AIAA Paper*, Vol. 420, 2000, pp. 10–13.

[15] Gern, F., Gundlach, J., Ko, A., Naghshineh-Pour, A., Sulaeman, E., Tetrault, P., Grossman, B., Kapania, R., Mason, W., Schetz, J., et al., "Multidisciplinary Design

Optimization of a Transonic Commercial Transport with a Strut-Braced Wing," *SAE Transactions*, Vol. 108, No. 1, 1999, pp. 1345–1355.

[16] Gern, F. H., Ko, A., Sulaeman, E., Gundlach, J. F., Kapania, R. K., and Haftka, R. T., "Multidisciplinary Design Optimization of a Transonic Commercial Transport with Strut-Braced Wing," *Journal of Aircraft*, Vol. 38, No. 6, 2001, pp. 1006–1014.

[17] Gur, O., Bhatia, M., Schetz, J. A., Mason, W. H., Kapania, R. K., and Mavris, D. N., "Design Optimization of a Truss-Braced-Wing Transonic Transport Aircraft," *Journal of Aircraft*, Vol. 47, No. 6, 2010, pp. 1907–1917.

[18] Norris, G., "Truss-Braced Wings May Find Place on Transonic Aircraft," *Aviation Week and Space Technology*, March 2016.

[19] Anderson, J. D., *Introduction to Flight*, Vol. 199, McGraw-Hill Boston, 2005.

[20] Hoerner, S. F. and Borst, H. V., "Fluid-Dynamic Lift: Practical Information on Aerodynamic and Hydrodynamic Lift," *NASA STI/Recon Technical Report A*, Vol. 76, 1975, pp. 32167.

[21] McCroskey, W., "A Critical Assessment of Wind Tunnel Results for the NACA 0012 Airfoil," Tech. rep., DTIC Document, 1987.

[22] Meadows, N. A., *Multidisciplinary Design Optimization of a Medium Range Transonic Truss-Braced Wing Transport Aircraft*, Master's thesis, Virginia Polytechnic Institute and State University, Blacksburg, VA, 2011.

[23] Sobieszczanski-Sobieski, J. and Haftka, R. T., "Multidisciplinary Aerospace Design Optimization: Survey of Recent Developments," *Structural Optimization*, Vol. 14, No. 1, 1997, pp. 1–23.

[24] Malone, B. and Papay, M., "ModelCenter: An Integration Environment for Simulation Based Design," *Simulation Interoperability Workshop*, 1999.

[25] Braslow, A., Maddalon, D., Bartlett, D., Wagner, R., and Collier, F., "Applied Aspects of Laminar-Flow Technology," *Viscous Drag Reduction in Boundary Layers*, Vol. 123, 1990, pp. 47.

[26] Malone, B. and Mason, W., "Multidisciplinary Optimization in Aircraft Design Using Analytic Technology Models," *Journal of Aircraft*, Vol. 32, No. 2, 1995, pp. 431–438.

[27] Mason, W., "Analytic Models for Technology Integration in Aircraft Design," *Rep./AIAA; 90-3262*, 1990.

[28] Hilton, W. F., *High-Speed Aerodynamics*, Longmans, Green, 1951.

[29] Tétrault, P.-A., Schetz, J. A., and Grossman, B., "Numerical Prediction of Interference Drag of Strut-Surface Intersection in Transonic Flow," *AIAA journal*, Vol. 39, No. 5, 2001, pp. 857–864.

[30] Duggirala, R. K., Roy, C. J., and Schetz, J. A., "Analysis of Interference Drag for Strut-Strut Interaction in Transonic Flow," *AIAA journal*, Vol. 49, No. 3, 2011, pp. 449–462.

[31] Zhang, G., Patuwo, B. E., and Hu, M. Y., "Forecasting with Artificial Neural Networks:: The State of the Art," *International Journal of Forecasting*, Vol. 14, No. 1, 1998, pp. 35–62.

[32] Irie, B. and Miyake, S., "Capabilities of Three-Layered Perceptrons," *Neural Networks, 1988., IEEE International Conference on*, IEEE, 1988, pp. 641–648.

[33] Kriesel, D., "A Brief Introduction on Neural Networks," 2007.

[34] Barron, A. R., "[Neural Networks: A Review from Statistical Perspective]: Comment," *Statistical Science*, Vol. 9, No. 1, 1994, pp. 33–35.

[35] Chiba, K., Oyama, A., Obayashi, S., Nakahashi, K., and Morino, H., "Multidisciplinary Design Optimization and Data Mining for Transonic Regional-Jet Wing," *Journal of Aircraft*, Vol. 44, No. 4, 2007, pp. 1100–1112.

[36] Palacios, F., Colonno, M. R., Aranake, A. C., Campos, A., Copeland, S. R., Economon, T. D., Lonkar, A. K., Lukaczyk, T. W., Taylor, T. W., and Alonso, J. J., "Stanford University Unstructured (SU2): An Open-Source Integrated Computational Environment for Multi-Physics Simulation and Design," *AIAA Paper*, Vol. 287, 2013, pp. 2013.

[37] Palacios, F., Economon, T. D., Aranake, A. C., Copeland, S. R., Lonkar, A. K., Lukaczyk, T. W., Manosalvas, D. E., Naik, K. R., Padrón, A. S., Tracey, B., et al., "Stanford University Unstructured (SU2): Open-Source Analysis and Design Technology for Turbulent Flows," *AIAA paper*, Vol. 243, 2014, pp. 13–17.

[38] Crouch, J., Garbaruk, A., Magidov, D., and Travin, A., "Origin of Transonic Buffet on Aerofoils," *Journal of Fluid Mechanics*, Vol. 628, 2009, pp. 357–369.

[39] Dole, C. E. and Lewis, J. E., *Flight theory and aerodynamics: a practical guide for operational safety*, John Wiley & Sons, 2000.

Appendix A

Tabulated CFD Results

Table A.1: Tabulated results from CFD used to create surrogate models

t/c	M	α (deg)	C_l	C_d	C_{dw}	$C_{m,\frac{1}{4}}$
0.06	0.7	3	0.858664	0.023616	0.018200	-0.096746
0.06	0.7	1.5	0.610992	0.011607	0.005765	-0.115383
0.06	0.7	0	0.380420	0.008329	0.002267	-0.120462
0.06	0.7	-1.5	0.144545	0.007709	0.001682	-0.119223
0.06	0.7	-3	-0.097726	0.008180	0.002376	-0.119311
0.06	0.8	1.5	0.867064	0.017588	0.011884	-0.167603
0.06	0.8	0	0.471654	0.010037	0.004153	-0.153904
0.06	0.8	-1.5	0.167362	0.008240	0.002409	-0.146407
0.06	0.8	-3	-0.182986	0.017444	0.012092	-0.138996
0.06	0.85	3	0.879568	0.060777	0.054253	-0.212276
0.06	0.85	1.5	0.698469	0.032673	0.026409	-0.191158
0.06	0.85	0	0.419567	0.019353	0.013286	-0.177601
0.06	0.85	-1.5	0.101846	0.016157	0.010489	-0.170096
0.06	0.85	-3	-0.330842	0.041823	0.037027	-0.075740
0.06	0.9	4.5	0.899310	0.106613	0.098916	-0.261988

0.06	0.9	3	0.734920	0.074644	0.066983	-0.240379
0.06	0.9	1.5	0.528232	0.049176	0.042001	-0.218081
0.06	0.9	0	0.180164	0.032987	0.026781	-0.158051
0.06	0.9	-1.5	-0.281263	0.052100	0.046314	-0.018486
0.06	0.95	6	0.922023	0.131458	0.124261	-0.260182
0.06	0.95	4.5	0.744995	0.094665	0.087448	-0.234849
0.06	0.95	3	0.495347	0.068747	0.061622	-0.182632
0.06	0.95	1.5	0.211571	0.056629	0.049446	-0.117660
0.06	0.95	0	-0.029403	0.055505	0.048296	-0.061223
0.08	0.7	3	0.872108	0.020270	0.014787	-0.097371
0.08	0.7	1.5	0.617203	0.010913	0.005058	-0.115495
0.08	0.7	0	0.377421	0.008823	0.002835	-0.118686
0.08	0.7	-1.5	0.135805	0.008228	0.002282	-0.117102
0.08	0.7	-3	-0.112021	0.008645	0.002912	-0.117037
0.08	0.8	3	0.925233	0.048401	0.042624	-0.170369
0.08	0.8	1.5	0.784954	0.022991	0.017292	-0.169869
0.08	0.8	0	0.473495	0.011691	0.005945	-0.155633
0.08	0.8	-1.5	0.151185	0.009233	0.003574	-0.144987
0.08	0.8	-3	-0.231655	0.022452	0.017380	-0.120990
0.08	0.85	4.5	0.916276	0.094344	0.087588	-0.208606
0.08	0.85	3	0.754968	0.060549	0.054022	-0.188034
0.08	0.85	1.5	0.568670	0.037592	0.031291	-0.178565
0.08	0.85	0	0.339710	0.023092	0.017116	-0.169001
0.08	0.85	-1.5	0.001726	0.024829	0.019627	-0.134483
0.08	0.9	4.5	0.822387	0.116912	0.108735	-0.259955
0.08	0.9	3	0.637061	0.086770	0.078939	-0.231737
0.08	0.9	1.5	0.315667	0.056231	0.049660	-0.148413
0.08	0.9	0	-0.073531	0.052903	0.046934	-0.030787

0.08	0.95	6	0.840509	0.139644	0.132021	-0.253995
0.08	0.95	4.5	0.585144	0.108379	0.100790	-0.186518
0.08	0.95	3	0.372590	0.087294	0.079650	-0.137674
0.08	0.95	1.5	0.166148	0.076626	0.068962	-0.097044
0.08	0.95	0	-0.033733	0.075261	0.067607	-0.051451
0.1	0.7	3	0.879792	0.018321	0.012563	-0.098137
0.1	0.7	1.5	0.619340	0.011086	0.004938	-0.114814
0.1	0.7	0	0.371850	0.009446	0.003190	-0.116477
0.1	0.7	-1.5	0.124939	0.008817	0.002597	-0.114666
0.1	0.7	-3	-0.128698	0.009428	0.003422	-0.114422
0.1	0.8	4.5	0.869695	0.073165	0.068093	-0.140025
0.1	0.8	3	0.788318	0.048215	0.042831	-0.149150
0.1	0.8	1.5	0.659055	0.029115	0.023447	-0.159485
0.1	0.8	0	0.437055	0.016202	0.010310	-0.155044
0.1	0.8	-1.5	0.123964	0.011196	0.005332	-0.143879
0.1	0.8	-3	-0.251006	0.030561	0.025404	-0.094381
0.1	0.85	6	0.931934	0.129827	0.124365	-0.199813
0.1	0.85	4.5	0.775387	0.091538	0.085987	-0.177781
0.1	0.85	3	0.600150	0.061223	0.055630	-0.159741
0.1	0.85	1.5	0.420530	0.041751	0.036172	-0.150321
0.1	0.85	0	0.173575	0.030883	0.025461	-0.128711
0.1	0.85	-1.5	-0.116589	0.043075	0.038094	-0.064932
0.1	0.9	6	0.889934	0.167149	0.161027	-0.269225
0.1	0.9	4.5	0.694807	0.134404	0.128220	-0.225979
0.1	0.9	3	0.341897	0.091492	0.085560	-0.101919
0.1	0.9	1.5	0.092751	0.076896	0.070924	-0.041907
0.1	0.9	0	-0.121274	0.081700	0.075544	0.002457
0.1	0.9	-1.5	-0.290440	0.101060	0.094631	0.022423

0.1	0.95	7.5	0.920168	0.191223	0.185476	-0.267429
0.1	0.95	6	0.679863	0.155001	0.149020	-0.196816
0.1	0.95	4.5	0.503345	0.128263	0.122069	-0.155529
0.1	0.95	3	0.326786	0.109766	0.103414	-0.122143
0.1	0.95	1.5	0.145319	0.099745	0.093274	-0.084948
0.1	0.95	0	-0.031714	0.098378	0.091836	-0.045461

Table A.2: Tabulated results from CFD used to validate surrogate models

t/c	M	α (deg)	C_l	C_d	C_{dw}	$C_{m,\frac{1}{4}}$
0.07	0.75	1	0.593468	0.010405	0.004516	-0.128465
0.07	0.75	2	0.798606	0.015286	0.009595	-0.114824
0.07	0.825	1	0.664761	0.022498	0.016565	-0.179174
0.07	0.825	2	0.804108	0.036306	0.030270	-0.184826
0.07	0.875	1	0.473097	0.036626	0.030080	-0.191671
0.07	0.875	2	0.635429	0.051910	0.045063	-0.208726
0.09	0.75	1	0.592759	0.010865	0.005085	-0.126573
0.09	0.75	2	0.807593	0.014488	0.008885	-0.117862
0.09	0.825	1	0.555546	0.028294	0.022382	-0.168221
0.09	0.825	2	0.665199	0.039134	0.033096	-0.165721
0.09	0.875	1	0.284146	0.042442	0.036348	-0.140153
0.09	0.875	2	0.451846	0.054456	0.047941	-0.164559